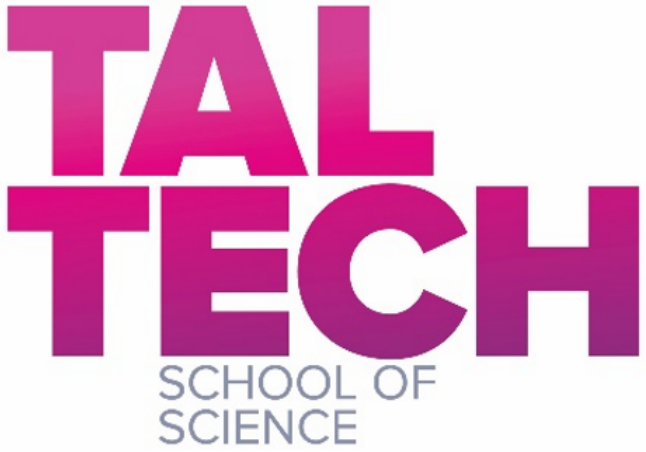

Irregularities seen in the electrical characteristics of a large array direct current Superconducting Quantum Interference Devices due to the deviations in the single cell parameters

Master's thesis

Student: Daniil Vili
Supervisors: Mikko Kiviranta, Principal Scientist (VTT)
Mihhail Klopov, Associate Professor (TalTech)
Study program: 182533YAFM, Applied Physics

2024

I hereby declare that I have written this thesis independently and the thesis has not previously been submitted for defence. All works and major viewpoints of the other authors, data from sources of literature and elsewhere used for writing this paper have been properly cited.

Daniil Vili

Digitally signed by Daniil Vili
Reason: I am the author of this document
Date: 2024.05.16 20:18:06 +03'00'

Author: Daniil Vili	Date

The thesis complies with the requirements for master's theses.

Mikko Kiviranta

Digitally signed by Mikko Kiviranta
DN: cn=Mikko Kiviranta, c=FI, o=VTT - Technology Research Centre of Finland, ou=Microelectronics and Quantum Technology, email=Mikko.Kiviranta@vtt.fi
Reason: I am approving this document
Date: 2024.05.16 21:01:22 +03'00'

Supervisor: Mikko Kiviranta	Date
Supervisor: Mihhail Klopov	Date

Contents

Abbreviations

ATHENA	Advanced Telescope for High-Energy Astrophysics
BCS	Bardeen-Cooper-Schrieffer
DC	Direct Current
Eq	Equation
FIB	Focused Ion Beam
Fig	Figure
GL	Ginzburg-Landau
IV	Current-Voltage
JJ	Josephson Junction
LNA	Low Noise Amplifier
RF	Radio Frequency
RSCJ	Resistively Capacitively Shunted Junction
SEM	Scanning Electron Microscope
SIS	Superconductor Insulator Superconductor
SQUID	Superconducting QUantum Interference Device
SWAPS	Sidewall-Passivating Spacer Structure
TES	Transition Edge Sensors
VTT	VTT Technical Research Centre of Finland
XRISM	X-Ray Imaging and Spectroscopy Mission
X-IFU	X-ray Integral Field Unit
Φ**V**	Flux-Voltage

Chapter 1

Introduction

Superconducting QUantum Interference Devices (SQUIDs) are known for the best magnetic sensitivity and the ability to operate at cryogenic temperatures, making them one of the best devices to measure low magnetic fields and flux. In addition, being the best magneto- and gradiometers, SQUIDs can also be used as cryogenic current to voltage amplifiers (transimpedance amplifiers), using magnetic coupling. In the past, SQUIDs have been used to measure gravitational waves [1], bio-magnetic fields (brain scanners) [2] and in the readout chain to detect radiation [3]. Conventionally, SQUIDs have found their application in the field, where the amplification of the small currents is required. For example, a combination of transition-edge sensor (TES) and VTT provided direct current SQUID (DC SQUID) readout chain technique will be used in the Advanced Telescope for High-Energy Astrophysics (ATHENA) space mission by European Space Agency (ESA), to detect X-rays.

The performance of the SQUID is determined by the noise level and the gain factor (transresistance/transimpedance). The gain shows how much voltage is generated across the SQUID per amount of applied flux, through the superconducting loop of the SQUID. In the real-life application, noise level is one important limiting factor in the SQUID performance, as it will have to be considered for the gain. One of the reasons to use array of SQUIDs rather than a single SQUID cell is the higher signal power. The basic performance of the SQUID can be analysed using IV- and ΦV- characteristics, the last used especially to determine the gain factor. Unfortunately, irregularities present in the IV- and ΦV- characteristic make the gain non-uniform and decrease the general performance of the SQUID. SQUID is an active nonlinear device, the performance is determined by the parameters, such as, shunt resistance of Jospehson Junctions (JJs), loop inductance, JJ capacitance and the external electrical circuit loading (impedance). These parameters, if not well considered in the design or measurement setup, will cause distortion in the IV- and ΦV- characteristics, leading to decrease in SQUID performance. In addition, understanding the cause of these irregularities can provide valuable feedback about the SQUID fabrication and bottlenecks of the fabrication process, thus improving the fabrication process and the yield.

The content of this thesis is split between seven main chapters. Chapter 2 gives an introduction into the superconductivity and SQUIDs. Chapter 3 explains the dynamics of Josephson Junctions. Chapter 4 gives more understanding about DC SQUIDs, main design parameters and explains IV-

and ΦV- characteristics. Chapter 5 concentrates on the analysis of the actual measured devices, observation of the degradatory mechanisms and introduces the model to simulate the critical current distribution. Chapter 6 interprets the results achieved by the model introduced for the critical current distribution, shows experimental data on the parasitic capacitance affect to SQUIDs and includes the discussion about the possible improvements. Followed by a brief conclusion of the work and suggestions for the further development in this field, Chapter 7.

In this thesis, irregularities in the response of the VTT DC SQUID arrays will be studied and analysed. For the analysis, IV- and ΦV- characteristic plots are used. The main irregularities discussed in this thesis are caused due to the critical current variation among the single SQUID cells in the SQUID array and parasitic capacitance due to the external circuitry. VTT thin film, niobium based DC SQUIDs are designed, fabricated and measured (full plots can be found in the Appendices) in the liquid helium at VTT.

Chapter 2

Superconductivity and Superconducting Quantum Interference Devices

2.1 Superconductivity

Introduction of the low-temperature physics field was pioneered by Dutch physicist Heike Kamerlingh Onnes, who was the first to liquefy, store and transfer liquid helium in the smaller amounts, in addition, to the previous work on liquid oxygen and hydrogen. The liquefaction of helium was achieved by Onnes and his team on 10^{th} of July 1908 [4], in his laboratory at Leiden University, Netherlands. The following years were spent on the improvement of cryogenics hardware and liquefaction process efficiency, which led to the discovery of a zero resistance phenomena, or as we know it today superconductivity. In his first experiments, Onnes characterised materials, such as platinum (used as thermometer), mercury, mercury-gold alloy, lead and tin at temperatures reaching down to 1.5K. Since these early experiments, scientists have discovered new emergent properties and categorized these superconductors along various classes, such as type I v.s. type II, or as low-temperature v.s. high-temperature. Here we should explain superconductivity as a property of the material to have zero electrical resistance and repel external electromagnetic fields from the bulk of the material.

In 1935, London Model gave a microscopic description and explained screening of electromagnetic fields from the interior of the a bulk superconductors, using Equation 2.1 (Eq. 2.1) and Eq. 2.2, i.e. the First and the Second London equation [5, 6]

$$\frac{\mathrm{d}\mathbf{J}_s}{\mathrm{d}t} = \frac{n_s {e^*}^2 \mathbf{E}}{m^*} \tag{2.1}$$

where $\mathbf{J_s}$ and n_s stand for the current and the number densities of the quasi-particles, respectively e^* and m^* being the charge and the mass of the quasi-particle in the applied electrical field $\mathbf{E}$

$$\nabla^2 \mathbf{B} = \frac{1}{\lambda_L^2} \mathbf{B} \tag{2.2}$$

$$\lambda_L^2 = \sqrt{\frac{m^*}{\mu_0 n_s e^{*2}}} \tag{2.3}$$

where $\mathbf{B}$ is the internal magnetic field and λ_L is so-called London penetration depth and μ_0 magnetic permeability. The first London equation shows that any applied electrical field accelerates quasi-particles, resulting in perfect conductivity. The second one explains so-called Meissner effect [1], that a magnetic field is exponentially screened from the interior of the bulk superconductor within the penetration depth λ_L resulting in the perfect diamagnetism. However, λ_L is only valid in an ideal theoretical limit $T \to T_0$, where T is temperature of the material and T_0 absolute zero. However, experiments have shown that actual penetration depths are larger. To solve that one would use characteristic length ξ_0, introduced by Alfred Brian Pippard

$$\xi_0 = a\frac{\hbar v_F}{kT_c} \tag{2.4}$$

where a is a numerical constant of the order of unity, $\hbar$ reduced Planck constant, v_F - Fermi velocity, k - Boltzmann constant and T_c - critical temperature of the superconducting material. Compared to the penetration depth λ_L, characteristic length ξ_0 considers the fact that the electrical field $\mathbf{E}$ of the superconductor is nonuniform, thus there will be a nonuniform distribution of the supercurrent, hence increasing superconducting penetration depths λ (always larger than λ_L) [2], following relation $\lambda \ll \xi_0$.

After the superconductivity was explained using the London Model, there was an emerge of GL (Ginzburg-Landau) Model and BCS (Bardeen-Cooper-Schrieffer) theory. GL Model was proposed in 1950, 7 years before BCS and is described as a limited form of BCS theory [5]. The main advantage of GL Model is the quantum-mechanical approach to the superconductivity, by introduction of the pseudowavefunction ψ, to describe superconducting electrons or quasi-particles. It allows to solve the nonlinear effects of strong electromagnetic fields and the spatial variation of quasi-particle density, which was not handled by London Model. In addition, GL Model introduces important GL parameter κ (Eq. 2.5), to distinguish type I from type II superconductors. Example of the materials and GL parameter numerical values, will be introduced under the Flux trapping section.

$$\kappa = \frac{\lambda}{\xi} \quad [3] \tag{2.5}$$

As mentioned above, the GL Model is a limited form of BCS theory, explaining the same phenomena, are approaching superconductivity phenomenologically, considering the laws of thermo-and electrodynamics, while being compared to the empirical data available [6]. BCS theory, however, is so far the most comprehensive description of the superconductive phenomena. It uses quantum mechanics to explain the formation of the Cooper pairs (electron pairs) which are the charge carriers in the superconductor. The formation of the Cooper pairs is explained using the electron-phonon coupling mechanism [6].

[1] Meissner effect, demonstrated by W. Meissner and R. Ochesenfeld in 1933. It was shown that when lead sample underwent a transition $T > T_c$ ($T_{c,lead} = 7.2K$) while exposed to a weak magnetic field, instead of trapping the magnetic flux inside the bulk, the field was expelled.

[2] λ_L is defined at $T = 0$ and it will diverge at T_c as described by $\lambda(T) \approx \lambda(0)[1 - (T/T_c)^4]^{-1/2}$.

[3] Here ξ is different from characteristic length ξ_0 and is actually called *temperature-dependent coherence length* or *Ginzburg-Landau coherence length* $\xi = \xi_{GL}$ [7].

2.2 Superconducting Quantum Interference Devices

SQUID is an active, nonlinear, device consisting of superconducting loop, including either one (Radio Frequency or RF SQUID) or more Josephson Junctions (JJs), such as for DC SQUID (two JJs) Figure 2.1 (Fig. 2.1), and superconducting coil(s).

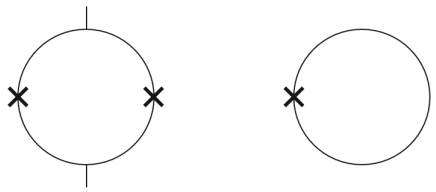

Figure 2.1: On the left is the electrical symbol for DC SQUID and on the right for RF SQUID. Crosses are JJs.

These devices have been mainly used as magneto-and gradiometers due to one of the best magnetic field noise and resolution characteristics. According to the literature, these devices can reach $fT/\sqrt{Hz}$ range in magnetic field noise and nT/Φ_0 in magnetic field sensitivity [8]. Apart from the direct use as magnetometer, SQUIDs can also be used as a current-voltage amplifier. For instance, this type of technology is being realised to be used on board the Large-class (L-class) mission by European Space Agency (ESA), called Advanced Telescope for High Energy Astrophysics (ATHENA) [9].

ATHENA mission is an observatory with the main objective to perform spectroscopy of the incoming X-rays, originating from e.g. black holes. To reach these objectives, the X-ray Integral Field Unit (X-IFU) instrument on board the mission, will include a primary (detection) and secondary (background noise) focal planes. Primary focal plane will use matrix of Transition Edge Sensors (TES) pixels for incoming X-ray detection, followed by the first stage of multiplexing SQUIDs and the second stage of SQUIDs, for the current to voltage amplification. Current produced by X-rays hitting TESs is in μA region, with its noise floor being in the $pA/\sqrt{Hz}$ region. Secondary focal plane will be used for background noise detection, having similar design as primary plane, but without multiplexing SQUIDs and TESs used are of different design. Using this type of, edge-cutting, technology the energy resolution of $2.5\ eV$ is set as a requirement for the X-ray detection of the ATHENA observatory. This will be ten times smaller compared to a similar existing observatory X-Ray Imaging and Spectroscopy Mission (XRISM). [9]

RF SQUID will not be handled in the context of this thesis, however, compared to DC SQUID, their fabrication is easier and it was the reason why in the earlier SQUID history they were more popular. The RF SQUID operation is based on the different operations modes, such as, hysteretic- and nonhysteretic exists - for the readers interest, more discussion regarding RF SQUIDs can be found in [10]. With the emerge of the thin-film based fabrication technology and lower noise characteristics [11], DC SQUIDs became more attractive to the research and in development of the new technologies.

DC SQUID has two parallel JJs with similar critical currents, which may be slightly different due to the fabrication for instance, connected via superconducting loop (SQUID loop). In practice, DC SQUID is biased close to the JJs critical current, if both JJs are identical then the critical current of the SQUID is equal to the sum of both JJ critical currents. If the biasing current of the SQUID is further increased, above the critical value, SQUID will switch from superconducting state to finite voltage state. If the external flux is applied, SQUID loop will generate so-called screening currents to cancel out the applied flux thus introducing self-induced flux. This phenomena is caused due to the quantization effect, as closed superconducting circuit can only contain a discrete number of magnetic flux, known as fluxon Φ_0 (sometimes referred to also as flux quantum/quanta), Eq. 2.6. More precisely, the magnetic field times the area of a closed superconducting loop must always be a multiple of $h/2e$ [12]. Another way to understand the quantization effect is based on the fact that the superconducting wavefunction of the superconducting loop has to be coherent and have integral number of wavefunction cycles around the loop. In other words, magnetically induced screening currents of the superconducting loop, keep the coherence of the wavefunction.

$$\Phi_0 = h/2e = 2.07 \times 10^{-15}\ [Wb] \tag{2.6}$$

These same magnetically induced screening currents will create in-balance between the currents through the JJs - change in the phase difference of each JJs. As a matter, when the external applied flux Φ_{ex} value equals to half integer of the flux quantum Φ_{ex} / $\Phi_0 = n + 1/2$, it is energetically advantageous for the screening current to change direction, as seen in the Fig. 2.2. When operating close to the critical current of the JJ, the screening currents drive one of the JJs to the normal state. Considering the above explained basic operation of the DC SQUID, very small currents can be measured, using DC SQUIDs as current to voltage amplifiers.

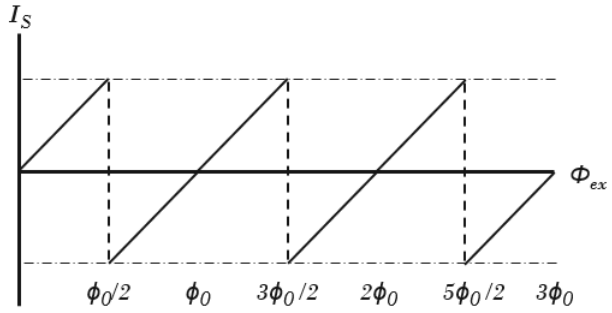

Figure 2.2: Screening current I_s and applied magnetic flux Φ_{ex}.

2.3 Cryogenic systems

Before proceeding onward with the more specific analysis of the DC SQUIDs, it would be important to get acquainted with the equipment needed to study not only SQUIDs but also other devices/components, requiring low temperature environment. As mentioned in the beginning of this chapter, an important start point for the low temperature physics was liquefaction of helium. Although, liquid nitrogen was available 10 years before, discovered by James Dewar [4], the liquid

[4] Dewar also invented a vacuum isolated flask (Dewar) to store cryogenic liquids.

helium [13]. It is clear that liquid nitrogen temperature is not low enough for the most of the low temperature superconductors. Niobium ($T_c \approx 9.5\ K$) is nowadays one of the most used superconducting materials, another material commonly used is aluminium ($T_c \approx 1.14\ K$) [14]. Another advantage of the low temperature measurements is the reduced thermal noise level [5].

Fig. 2.3 shows the phase diagrams of two stable helium isotopes, Helium-4 (He^4) and Helium-3 (He^3). Understanding of these phase diagrams allows to explain different cooling techniques to reach sub-and millikelvin temperatures. Phase diagrams of the He^4 and He^3 isotopes shows that pure He^3 exists in the liquid state all the way down to the absolute zero, though at extremely low temperature around $2\ mK$ it turns into the superfluid [6] [16]. He^4 however exists as a mixture including also He^3 component, thus it has two different phases so-called He I and He II with he $T_c = 2.17\ K$.

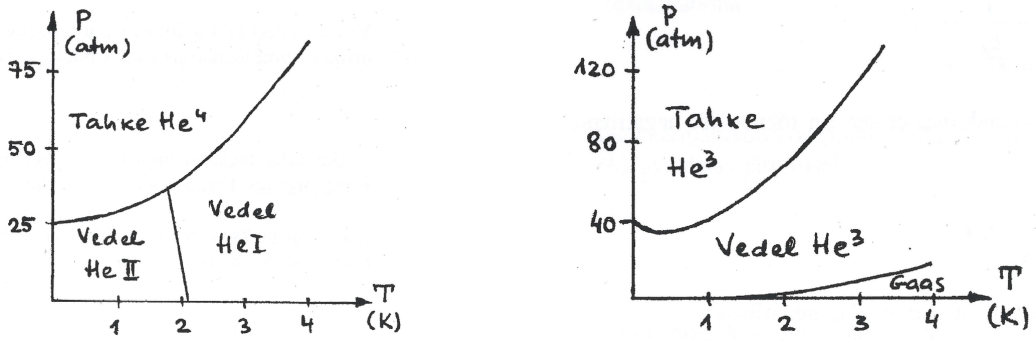

Figure 2.3: He^4 phase diagram with He I and He II phases (left). He^3 phase diagram (right). *Tahke, Vedel* and *Gaas*, respectively meaning solid, liquid and gas states [16].

Cooling systems may be divided into the wet and dry systems/refrigerators. The easiest example of the wet fridge is *Dewar*, filled with liquid He^4 providing $4.2\ K$ cryogenic environment (operating in the He I liquid phase). To reduce the temperature even more (down to $2.17\ K$) a pump has to be used to increase the evaporation rate of the liquid helium. For *Dewar* measurements, sample is attached on the dipsticks (Fig. 2.4) cold head and immersed into the liquid helium. Dipstick is a tool used to immerse and keep the sample inside the *Dewar*. Setup of *Dewar* and dipstick is shown in Appendix 1.

Figure 2.4: Dipstick for SQUID measurements in VTT. One the left is a plastic cold head for attaching the sample and connecting it to the signal lines, going through the narrow tube all the way to the right, through the feed through, to the room temperature electronics.

For the lower temperatures, such as mK range, one of the techniques is to use dilution refrigera-

[5] Johnson–Nyquist noise power spectral density $\overline{v_n^2} = 4k_BTR$ [15].

[6] Superfluid is a state when a liquid has zero dynamic viscosity, which allows it to flow through any small physical gap. Both He^4 and He^3 turn into Bose-Einstein condensate, creating superfluid.

tors. Dilution refrigerators operate on the principle of the phase separation of the He^4 and He^3 helium isotopes mixture. As seen from the Fig. 2.5, the phase diagram of He^4/He^3 mixture has a tricritical point. At temperatures below the tricritical point, mixture separates into He^3 rich phase and He^4 rich phase (dilute phase, hence called dilution refrigeration). These two phases have different densities, forcing the He^3 rich phase to float above the dilute phase. The cooling power of dilution refrigerators is achieved when He^3 atoms are transferred from the He^3 rich phase to the dilute phase by pumping on the mixture [6]. An example of operation schematics of the wet dilution refrigerator can be seen in the Appendix 2. Use of dilution refrigerator nowadays has become popular, for instance, it is one of the cooling systems chosen for the quantum computers. In addition to the mK temperature range, at the lowest point of operation, dilution refrigerators provide also stages where temperatures like $\approx 1\ K$ and $\approx 4\ K$ can be achieved, which is favorable to understand how SQUID characteristics change at different temperatures.

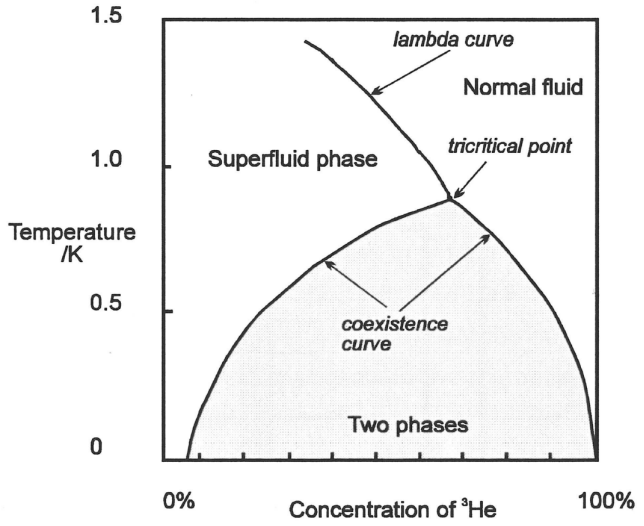

Figure 2.5: Phase diagram of He^4/He^3 mixture [17].

Chapter 3

Josephson Junctions

Josephson Junction (JJ) is an active device, where an insulator between two superconductors creates a weak link which allows Cooper pairs to pass from one superconductor to another, resulting in supercurrent. Here the weak link is referred to the state, where a slight overlap of the electron pair wavefunctions ψ_i of the two superconductors occurs. Even if there is no voltage or current biasing applied across the JJ, with the small-enough separation between superconductors, and with the quantum phase difference ϕ present, Cooper pair tunnelling will result in supercurrent. Cooper pair tunnelling can only take place when energy associated with the coupling exceeds the energy of the thermal fluctuations [7]. One way to generate the quantum phase difference in experiments, is to apply magnetic field.

To begin with the dynamics of the JJs, it is important to explain Josephson relations. The first relation (Eq. 3.1), shows that the current density J of the JJ has a maximum value of J_c, being the critical current density and the current density will vary with the phase difference ϕ of the two superconductors

$$J = J_c \sin \phi \tag{3.1}$$

By knowing the effective area A of a junction we can rewrite Eq. 3.1 in terms of the critical current $I = I_c \sin \phi$. If the current is increased above the critical current, $I > I_c$ and finite voltage is generated across the JJ, the phase difference ϕ would evolve according to

$$\frac{\partial \phi}{\partial t} = \frac{2e}{\hbar} V \tag{3.2}$$

where $2e$ represents the charge of the electron pair. When the finite voltage is generated across JJ, the wavefunctions, describing electron pairs, will become uncoupled and begin to slip relative to each other at a rate determined by Eq. 3.2 [7], known as Josephson frequency f_J (Eq. 3.4). In addition to electron pair tunneling, at non-zero voltage, there is also quasiparticle current. Eq. 3.1 is known as DC effect of JJ and Eq. 3.2 describes the AC effect in the JJs.

3.1 Critical current

From the JJ relations Eq. 3.1 and Eq. 3.2, a few important critical parameters for the junction characterisation can be derived and explained. The choice of these parameters will determine also

the operation of the SQUID. Maximum zero-voltage current density can be described by Eq. 3.3, so-called Ambegaokar-Baratoff relation [18]

$$J_{ctu} = G_n \left(\frac{\pi \Delta(T)}{2e} \right) \tanh \frac{\Delta(T)}{2k_B T} \tag{3.3}$$

where G_n is the tunnelling conductance [1] for $V \gg 2\Delta/e$ (relation $V_g = 2\Delta/e$ is called gap voltage) and Δ is a gap parameter. Gap voltage describes the binding energy of the Cooper pairs, thus when the potential difference of $2\Delta/e$ is reached, there is enough energy in the system to start breaking the Cooper pairs [2]. Tunnelling conductance G_n can also be interpreted as the inverse of the JJs normal state resistance R_n. Critical current density, is the critical current per unit area, and it is a property of the dielectric sheet, through which Cooper pairs tunnel, and out of which the Josephson junctions are formed. Above the critical current, junction will start experiencing finite voltage oscillations [3] expressed by the Josephson frequency f_J (angular frequency ω_J) [7]

$$f_J = \frac{w_J}{2\pi} = \left(\frac{1}{2\pi} \right) \frac{2e}{\hbar} V \tag{3.4}$$

The Josephson oscillations described by Eq. 3.4 are high frequency, reaching GHz bandwidth and with the peak occurring at the applied DC voltage $2\Delta/e$. The time average voltage response of these oscillations is actually the finite state voltage response generated by the JJ in the normal state. The gap parameter in the Ambegaokar-Baratoff relation (Eq. 3.3) is the energy needed for the quasiparticles to move from ground state to the lowest level of the excitation states, in addition, binding energy of each electron pair is 2Δ [7]. At $T = 0$ gap energy can be found using

$$\Delta = 2\hbar\omega_D e^{-1/N(0)V} \tag{3.5}$$

where $N(0)$ is density of the states at the Fermi surface, V is scattering amplitude and ω_D is *Debye* frequency. Eq. 3.6 shows the gap parameter temperature dependency, for both weak-and strong-coupled (Fig. 3.1) superconductors.

Metal	Tunneling experiment	Weak-coupling theory (error)	Strong-coupling theory (error)
Hg	4.61	3.53 (+31%)	4.50 (+ 2%)
In	3.69	3.53 (+ 5%)	3.87 (– 5%)
Nb	3.80	3.53 (+ 8%)	3.83 (– 1%)
Pb	4.50	3.53 (+27%)	4.47 (+ 1%)
Sn	3.74	3.53 (+ 6%)	3.73 (+ 0%)
Tl	3.60	3.53 (+ 2%)	3.71 (– 3%)

Figure 3.1: Measured and calculated values of $2\Delta/k_B T_c$. The errors indicate the necessary corrections required to obtain the experimental result [19].

[1] Tunnelling conductance G_n is normal metal to normal metal tunnelling conductance of the junction express by the formula $G_n = (2\pi e^2 A/\hbar) \mid T \mid^2 N_1(0) N_r(0)$, where N_l and N_r represent density of excitation states of the both electrodes forming the junction, so-called left and right electrode densities.

[2] For $V < V_g$, only quasiparticle tunneling takes place, in the case of superconductor-insulator-superconductor (SIS) junction [5].

[3] More precisely, these are sinusoidal supercurrent oscillations, which in the presence of additional elements, such as, shunt resistance, generate voltage oscillations.

$$2\Delta = 3.52 k_B T_c \quad [4] \tag{3.6}$$

Generally speaking, for the metallic superconductors the value, before k_B in Eq. 3.6, changes within the limit of $\pm 30\%$. For instance, at $T = 0$ aluminium has a gap energy of $0.34\ meV$ and niobium $3.05\ meV$ [14] - values presented are calculated for 2Δ. As the gap parameter is temperature dependent, by changing the temperature, critical current density of the JJ changes also. Fig. 3.2 shows the experimental data of the DC SQUID array ($Nb/Al/AlO_x/Nb$ trilayer JJ), measured at $4.2\ K$ and $800\ mK$. It was found by [20] that the gap voltage of $Nb/Al/AlO_x/Nb$ trilayer JJ to be $\Delta = (1.4 \pm 0.1)\ mV$ at $4.2\ K$.

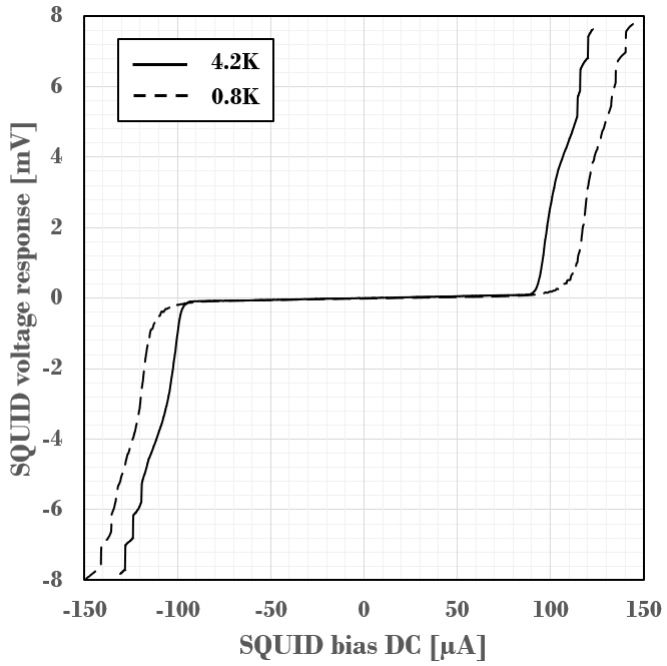

Figure 3.2: 4x40 SQUID array IV characteristics at $4.2\ K$ and $800\ mK$.

From Fig. 3.2 the critical current for $4.2\ K$ measurement is $92\ \mu A$ and for $0.8\ K$, $110\ \mu A$. Taking the ratio of the two critical currents we get 1.2. As a first order approximation, we could compare the analytical values using Eq. 3.3, choosing the gap energy for $800\ mK$ case to be $1.5\ meV$ (theoretical value for niobium at $T = 0$) and for $4.2\ K$, $1.4\ meV$ ($Nb/Al/AlO_x/Nb$ trilayer). The according ratio of the two critical current densities is 1.1, which is quite close to the ratio of the critical currents. However, that is just a simple example and for more accurate answer one should use the gap energy of $Nb/Al/AlO_x/Nb$ trilayer, measured at $800\ mK$.

3.2 Shunt resistance and capacitance

To get a better picture of the JJ dynamics, there would be a need for a model, which would include both the superconducting and the finite-voltage states of the JJ, as described by Eq. 3.1 and 3.2. One such model was suggested by D. E. McCumber [21] and W. C. Stewart [22],

[4] This is normalized form of the general approximation of the gap parameter $\Delta(T) \cong 3.2 k_B T_c (1 - T/T_c)^{1/2}$ at $T = 0$ as the gap vanishes when temperature approaches T_c.

so-called Resistively Capacitively Shunted Junction (RSCJ) model. RSCJ equivalent schematic is shown in the Fig. 3.3 and the analytical model below

$$I = I_c \sin\phi + \frac{\hbar}{2e}\frac{1}{R}\frac{d\phi}{dt} + \frac{\hbar}{2e}C\frac{d^2\phi}{dt^2} + I_n \tag{3.7}$$

where R is the total JJ resistance consisting of quasiparticle and external shunt resistances (in parallel), C is the capacitance across the JJ and I_n is the thermal noise current of the resistance [10].

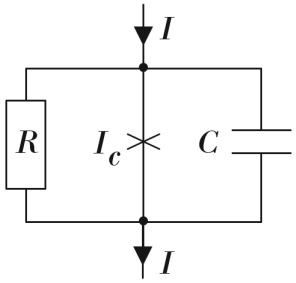

Figure 3.3: Schematics of the RSCJ model for one JJ. I is total current through the SQUID.

Eq. 3.7 is a nonlinear differential equation of the second order and one way to analyze it, is to solve numerically, however, this is not part of this thesis. On the other hand, if we introduce changes, such as, dimensionless time $t^* = (2\pi I_c R/\Phi_0)t$ and parameter $\beta_c = 2\pi I_c R^2 C/\Phi_0$ we can rewrite Eq. 3.7 to a dimensionless form

$$\beta_c\frac{d^2\phi}{dt^{*2}} + \frac{d\phi}{dt*} = -\frac{d}{d\phi}(-i\phi - \cos\phi) + i_n(t^*) \tag{3.8}$$

which is similar to the equation of motion of a particle in the force field. Particle mass being β_c, external force field described by the potential energy $-i\phi - \cos\phi$ and the time dependent change produced in this case by thermal fluctuations $i_n(t^*)$. It has been mentioned by [10], that if the thermal fluctuations are neglected, the average voltage response of JJ is hysteretic when $\beta_c > 0.7$ and nonhysteretic when $\beta_c < 0.7$. We will come back to the analysis of the RSJ model in the next Chapter.

3.3 Flux trapping

In the section 2.1 we introduced GL parameter κ, which draws a line between type I and type II superconductors as follows

$$\kappa \begin{cases} < 1/\sqrt{2}, & \text{type I} \\ > 1/\sqrt{2}, & \text{type II} \end{cases} \tag{3.9}$$

To explain the flux trapping phenomena, it is first important to mention that type I superconductors allow no flux penetration deeper than the penetration depth λ, inside the sample. At the critical external applied field H_c the transition from normal to the superconducting state is sharp (Fig. 3.4) - Meissner effect. However, type II superconductors experience Meissner effect until a certain lower magnetic field value, after which their superconductivity is defined as an intermediate, inhomogeneous, state between lower H_{c1} and upper critical field H_{c2} and is referred

to as mixed state (Fig. 3.4). In mixed state, material will experience a total flux expulsion until the H_{c1}, then some of the flux will start penetrating the material, using vortices of supercurrent.

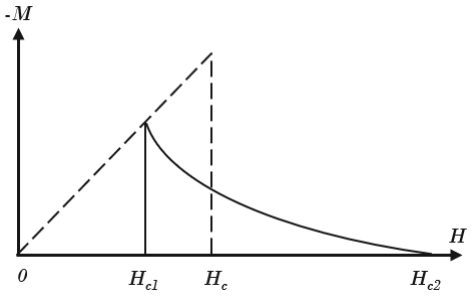

Figure 3.4: Graphical representation of the phase transitions between normal and superconducting states. Transition $0 \rightarrow H_c$ is Meissner effect and $H_{c1} \rightarrow H_{c2}$ mixed state.

In this thesis we are interested in type II superconductors, as the VTT DC SQUID arrays use thin film niobium, as the main superconductor material. Firstly, few vortices start to form at lower critical field H_{c1}, as it is energetically more favourable to have local exclusion of magnetic flux than a total exclusion. The maximum current density, generating the vortices, is achieved not in the centre of the superconductor, but at the value where radius equals to twice the ξ_{GL}. In other words, superconducting currents are generated both on the vortex walls and on the surface of the superconductor, whereas in type I currents are only generated on the surface of the superconductor. When the magnetic field is approaching upper critical field value of H_{c2}, the number of vortices increases to the limit where material goes normal, as the magnetic flux penetrates the bulk of material uniformly. Vortices are subjected to Lorentz force, which can exceed the pinning force, which is excess force keeping vortices steady in one place due to chemical or physical defects of the superconductor. As a result, vortices will start drifting around, generating resistance and dissipating heat.

In reality design geometries or material inhomogeneities can affect SQUID performance by reducing the ability to expel the magnetic field. Inhomogeneities cause type II superconductors to experience flux penetration (pinning sites) near T_c [23], thus locally braking the Meissner effect. As described by [24], defect sites present pinning force on the vortices leading to the hysteretic behaviour and after T_c, this force prevents vortices from leaving the material - flux trapping. As later seen from the experimental data, one way to get rid of flux trapping is to simply heat the SQUID above the T_c and let it cool down again. However, if the environments magnetic field is above the lower or higher critical values then that would require physical shielding, shielded room or implementing design rules which can prevent flux pinning to certain value. For instance, $1\ \mu m$ wide superconducting stripe gives a flux tolerance of $2\ mT$ [24], for comparison Earth's magnetic field strength ranges $25 - 65\ \mu T$.

3.4 Fabrication at VTT

Forming a weak link between two metallic superconductors e.g. niobium, can be done using another metal (such as aluminium) or semiconductor links, grain boundaries or insulating tunnel barriers (dielectrics such as aluminium or silicon oxides). Already mentioned in the section 3.1, SQUIDs measured in the frame of this thesis are using $Nb/Al/AlO_x/Nb$ trilayer structure to make the JJs. Two ways of fabricating JJs at VTT are pillar based, Fig. 3.5(a) and Sidewall-Passivating Spacer Structure (SWAPS, Fig. 3.5(b)) based designs. The core of the JJ fabrication is the realization of the trilayer, which sets the critical current I_c of the JJ. Trilayer is a design structure consisting of dielectric tunnel barrier layer between two electrodes layer, forming a weak link. For the pillar type JJ in Fig. 3.5(a), trilayer consists of the base electrode, tunnel barrier and counter electrode - forming NB2 layer. For SWAPS type design, trilayer is the same as for pillar type, but is called NB1 layer. For pillar type design, JJ size is defined with the remaining un-etched part of counter electrode (Fig. 3.5(a) CER) and for SWAPS based design, JJ is formed at the area of the crossing of NB1J and NB1 [25], Fig. 3.5(b). For the both fabrication technologies tunnel barrier is done using aluminium whose surface is oxidized into aluminium oxide. The advantage of SWAPS type design, for SQUID operation, is low parasitic capacitance [25]. In addition, from the SQUID design perspective, SWAPS fabrication process enables smaller JJ size than pillar type - denser chip layouts. For comparison, pillar type JJ with diameter of $3.2\ \mu m$ [26] and SWAPS type with $0.2\ \mu m\ \times\ 0.2\ \mu m$ [25].

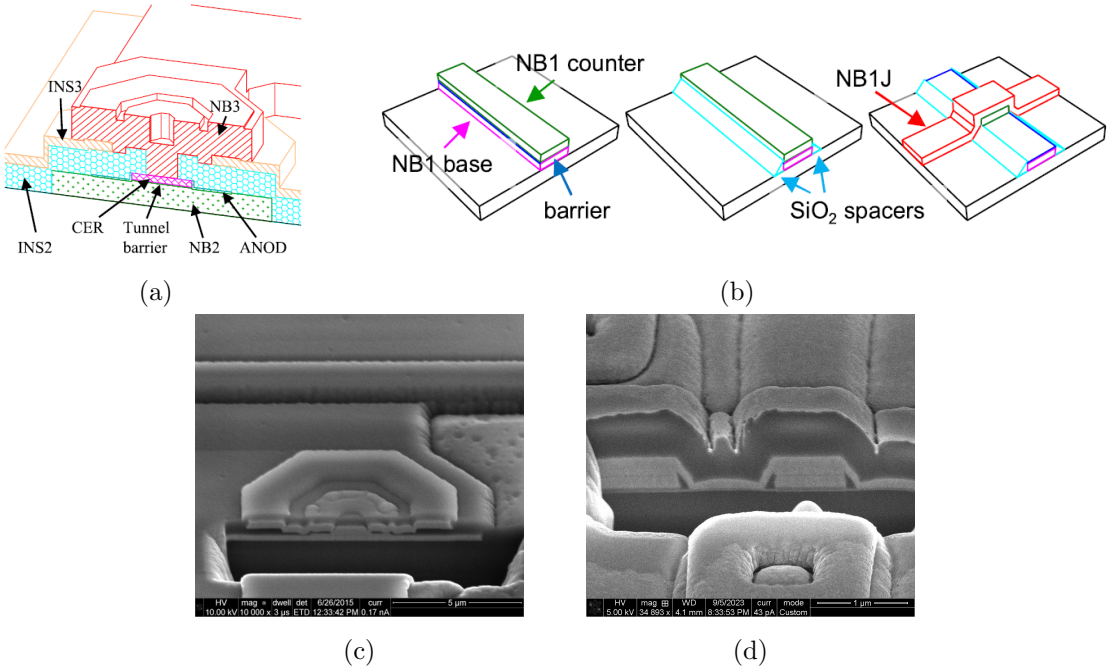

(a) (b)

(c) (d)

Figure 3.5: (a) and (c) pillar type JJ: NB2/3 niobium electrodes, INS2/3 SiO_2 insulation, CER (*Counter Electrode Removal*, the remaining un-etched part of NB3), ANOD sidewall anodization, *Tunnel barrier* (aluminium with oxidized surface) [26]. (b) and (d) SWAPS type JJ: NB1/1J niobium conductors, *barrier* (aluminium with oxidized surface) [27]. (c) and (d) were dissected with focused ion beam etching to reveal (a) and (b) thin film stacks.

Chapter 4

Direct Current Superconducting Quantum Interference Devices

In the following chapters, the notation of SQUID will be used instead of DC SQUID, as only DC SQUIDs will be analyzed. The latest development in field of SQUIDs has been thin-film based, multi-turn coil(s), planar washer (also referred to as SQUID loop) integrated circuits, manufactured on silicon wafers. The main materials for the low temperature devices being niobium or aluminium and for the high temperature ones yttrium-barium-copper-oxide (YBCO). Independent of the material choice, main SQUID components are superconducting loop (SQUID loop), two resistive shunts and two JJs in parallel. So-called coupled (sometimes referred to as flux-transformer coupling) and uncoupled (bare) designs exist - Fig. 4.1.

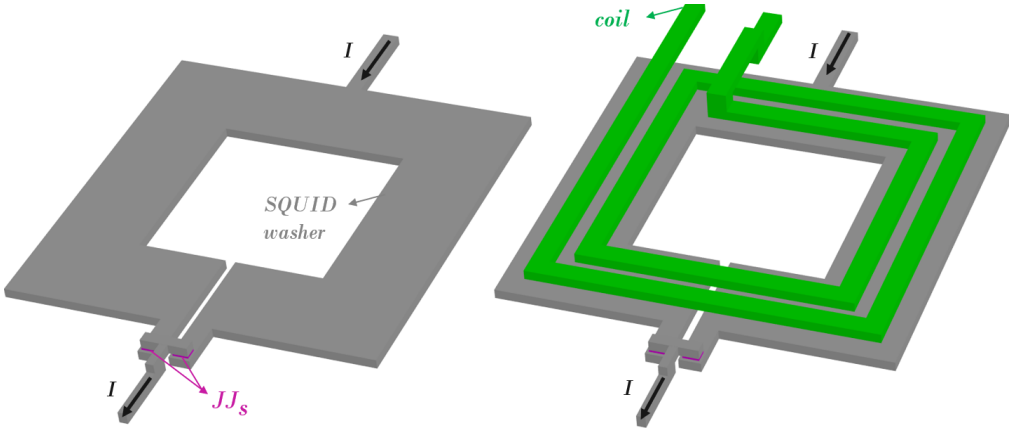

Figure 4.1: Simplified models of uncoupled SQUID (left) and one coil coupled SQUID (right). Grey area, between biasing current end is SQUID loop/washer.

So-called coupled SQUID designs involve a coil on top of the SQUID loop, called the 'input coil'. The coil would generate the sensed flux, either directly from the coil current when the SQUID is used as an ammeter, or as a part of the so-called flux-transformer circuit when the SQUID is used as a magnetometer. A flux-transformer would also include the so-called pick-up loop. Uncoupled or bare SQUID designs exist, too, but those can only be used as magnetometers, and are most commonly implemented as high temperature superconductor SQUIDs where multilayer deposition is technically challenging.

Introduction of the superconducting coil facilitates the ammeter configuration, and in the magnetometer configuration the flux-transformer would lower the magnetic field noise, or equivalently improves magnetic field resolution [8]. In the flux-transformer -based magnetometer configuration, the effective SQUID loop inductance would reduce by $40 - 50\%$ relative to the geometrical inductance, due to screening currents which flow in the input coil – pickup loop combination. For the both variants, there is a possibility of a strong LC resonance [8], degrading the performance. These resonance are worse for coupled SQUID. Even in the bare SQUID there exists the fundamental LC resonance of the washer and the junctions, but in a coupled SQUID the resonance structure is more complicated due to the complex electromagnetic interplay between the SQUID loop and the input coil. It is usually necessary to use resistive damping to lower Q-factor of the resonances, even if this leads to injection of additional thermal noise to the SQUID circuit. Finding the best balance between damping resonances and the injected thermal noise is bread and butter of design of a coupled SQUID. In the simplest approximation, the complex interplay between the input coil and SQUID washer can be lumped into the concept of parasitic capacitance, which would in the SQUID model appear across the SQUID loop inductance. The disadvantage of a coupled SQUID variant is the need for complex multilayer fabrication, which in case of high temperature superconductors may even be prohibitive. The coupled SQUID variant is however the only practical way to construct ammeters, in other words current sensors.

A fundamental figure of merit for SQUID is the noise energy resolution [8]

$$\varepsilon = S_\Phi(f)/(2L) \tag{4.1}$$

where L is the inductance of the SQUID, f frequency and $S_\Phi(f)$ power spectral density as seen below

$$S_\Phi(f) = S_V(f)/(\partial V/\partial \Phi_{ex})^2 \tag{4.2}$$

where $S_V(f)$ is the voltage noise power spectral density and $(\partial V/\partial \Phi_{ex})$ flux-to-voltage transfer function, sometimes referred to as the gain. Eq. 4.1 together with Eq. 4.2 give an insight into the nonlinear dynamics of the SQUID, where a certain balance between design parameters should be found. For instance, voltage noise power spectral density $S_V(f)$ is thermal noise, depending on the temperature T of the environment and the resistance (mostly contributed by the shunt resistors of the JJs). The transfer function, as will be analyzed later, depends on capacitance, inductance and their parasitics. However, for a certain case [1], the optimal energy resolution for the autonomous SQUID can be found from [10]

$$\varepsilon = S_\Phi(f)/(2L) \cong 12 k_B T \sqrt{LC} \tag{4.3}$$

where k_B is Boltzmann's constant.

[1] This applies for the case where the modulation parameter β_L and JJ damping parameter β_c are related as $\beta_L \cong \beta_c \cong 1$.

4.1 Single and arrays

Previous section gave an insight in to the importance of choosing carefully SQUID design parameters, to avoid the degradation in the performance. In addition to JJ design parameters, the SQUID chip design includes coil(s) to generate flux, filters (such as RC filtering), impedance matching structures and network of superconducting traces to connect all the parts (single SQUID cells), which may have additional unidealities. All these parts of the microelectronics circuitry have to be considered, as depending on the electrical circuit or even the operation environment, SQUID performance may be limited. In perfect case, all the single SQUID cells, forming the array, would be coherent. Meaning that each single SQUID cell is not affected by the other cells and parasitics, resulting in the "clean" contribution to the sum of the SQUID array. In addition, the total voltage is a sum of the SQUID cells in series and the total current is the sum of the parallel SQUID cells in series.

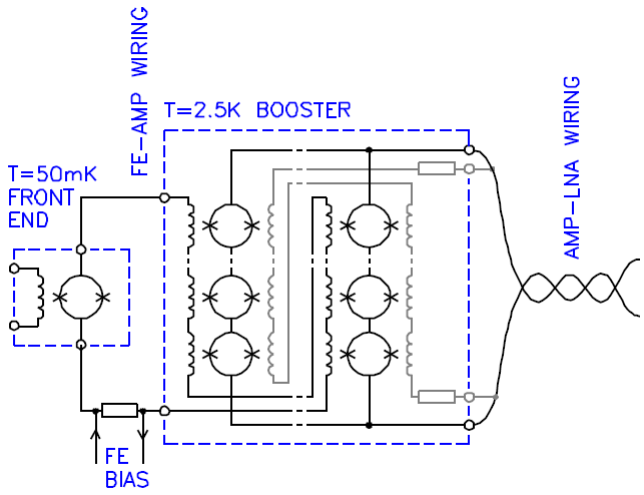

Figure 4.2: two-stage SQUID amplifier electrical circuit [27].

Fig. 4.2 shows a two-stage (so-called tandem) SQUID amplifier, consisting of the single cell SQUID (Frontend) and the SQUID array (Booster). Main difference between single and array designs is the number of SQUID cells included. Let us here define that one SQUID cell has two parallel JJs, integrated inside the SQUID loop, accompanied with the flux generating coil(s). Straight forward explained, SQUID arrays contains more than one SQUID cells, which can be integrated into the parallel and series SQUID arrays. When operating in the range of $0.05 - 4.2\ K$ one must bear in mind the cooling budget available to keep devices in the superconducting mode. According to [27], Frontend type SQUID may dissipate $\approx 1\ nW$ and Booster $\approx 200\ nW$ of heat. When immersed in liquid helium, the cooling budget may not be an issue as it will only increase the boil off due to the low latent heat of the liquid helium. However, for the dilution refrigerator operation, one has to be careful, as different stages have a certain cooling budget and if exceeded, one may not reach the desired operation temperature and even worse, cause the damage to the expensive scientific equipment. For instance the BlueFors LD400 dry dilution refrigerator, can provide $14\ \mu W$ cooling power at $T = 20\ mK$ and almost $0.5\ W$ at $2.5\ K$ [28], huge numbers

relative to the SQUID dissipation levels estimated above. Still, in multi-channel detector readout systems the above dissipation numbers must be multiplied by the number of channels, so that the total dissipation may in some cases become prohibitive. The situation is still worse in space missions, where electrical power consumed by the refrigerator must be generated by solar panels, and the refrigerator-generated heat must be radiated to space. The planned refrigerator for the X-IFU instrument, for instance, provides the total cooling capability of $1\ \mu W$ at $50\ mK$, only a fraction of which is allocated for SQUID cooling [9].

One of the main advantage of the SQUID arrays is the gain. If the SQUID cells are arranged in series or parallel, respectively the voltages sum up or stay the same, thus the gain is also dependent on the arrangement of the single cells. However, even if the devices are superconducting then the limiting factor may be the impedance and the noise level relative to the SQUID input, causing the reduction in the energy resolution.

4.2 Electrical characteristics

In this chapter we should introduce an analytical model to study the electrical characteristics of SQUID. Fig. 4.3 is a visual representation of the basic operation of the SQUID.

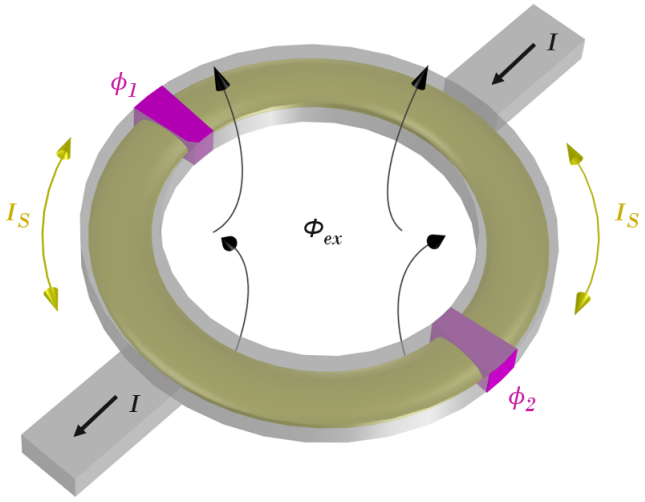

Figure 4.3: SQUID cell with two JJs (phase differences ϕ_1 and ϕ_1), changing induced screening current I_s and Φ_{ex} is applied external flux.

Total current through the SQUID in Fig. 4.3 can be written as

$$I = I_1 + I_2 \pm I_s = I_{c1} \sin \phi_1 + I_{c2} \sin \phi_2 \pm I_s \tag{4.4}$$

where I_1 and I_2 are respectively currents through the first JJ with phase difference ϕ_1 and the second JJ accordingly ϕ_2. Both junctions have critical currents $I_{c1,c2}$, which we will assume to be equal $I_{c1} = I_{c2} = I_c$. Fig. 2.2 shows the induced current changing the direction with the periodicity of the external flux $\Phi_{ex} = \Phi_0\ (n + 1/2)$. This sets also constraint regarding how the phase differences of the two JJs can change, to keep the coherence of the wavefunction across the superconducting loop. Relation, for the phase differences to keep the wavefunction coherence, is

found by taking the line integral in the center of the superconducting loop, in the vector field A

$$\phi_2 - \phi_1 = \frac{2e}{\hbar} \oint Adl = 2\pi\Phi/\Phi_0 \tag{4.5}$$

where Φ is the total flux. After rearranging Eq. 4.5 for ϕ_1 as variable, replacing it into Eq. 4.4 and neglecting the screening current induced flux ($\Phi = \Phi_{ex}$), we can maximize Eq. 4.4 in relation to ϕ_1. Result is a relation describing the total current through SQUID, depending on the applied flux Φ_{ex}

$$I(\Phi_{ex}) = 2I_c \left| \cos\left(\frac{\pi\Phi_{ex}}{\Phi_0}\right) \right| \tag{4.6}$$

Eq. 4.6 gives us periodic, rectified sinusoidal response with the maximum value at full and minimum value at half integer of the flux quanta - current modulation through the SQUID. However, Eq. 4.6 is still missing the contribution to the total applied flux from the flux induced by the screening current, so-called self-induced flux. Self-induced flux is caused due to the circulating currents acting against applied field to keep the coherence of the wavefunction. Applied magnetic flux Φ_{ex} breaks the symmetry of the total currents through each of the SQUID loop halves ($I_1 \neq I_2$), however, the critical currents are still assumed to have similar value $I_{c1} = I_{c2} = I_c$. As a result, total applied flux Φ is a sum of external magnetic field Φ_{ex} and induced field Φ_s

$$\Phi_s = LI_s = \frac{1}{2}L(I_2 - I_1) = \frac{1}{2}LI_c(\sin\phi_2 - \sin\phi_1) \tag{4.7}$$

$$\Phi = \Phi_{ex} + \frac{1}{2}LI_c(\sin\phi_2 - \sin\phi_1) \tag{4.8}$$

using Eq. 4.8 together with Eq. 4.5 we get

$$\phi_2 - \phi_1 = 2\pi/\Phi_0 \left[\Phi_{ex} + \frac{1}{2}LI_c(\sin\phi_2 - \sin\phi_1)\right] \tag{4.9}$$

By introducing the component of induced screening the total applied flux may be hysteretic. To avoid magnetic hysteresis, screening parameter β_L is used

$$\beta_L = \frac{2LI_c}{\Phi_0} \tag{4.10}$$

Screening parameter is also sometimes referred to as modulation parameter - it shows the modulation depth of the zero-voltage current as a function of applied total flux. As suggested by [8], for $\beta_L \gg 1$ modulation depth is very much smaller than $2I_c$, while for $\beta_L \ll 1$ it approaches the maximum value of $2I_c$. To avoid magnetic hysteresis $\beta_L \sim 1$, however, for the operation of the SQUID we have to consider that the SQUID inductance and critical current have finite values and finding an optimal selection for β_L is part of the design work.

4.2.1 Resistively Capacitively Shunted Junction for Direct Current Superconducting Quantum Interference Devices

In previous section we collected the analytical forms concerning the total current through the SQUID, total applied flux and received understanding on how the current modulation is achieved. Second part of the SQUID operation is to understand the finite voltage state region, where the SQUID leaves the superconducting stage described by the first Josephson relation Eq. 3.1 and

enters finite voltage state described by the second Josephson relation Eq. 3.2 - AC effect.

To describe the AC effect of the SQUID we will use RCSJ model (introduced partly under the section 3.2) as seen in the Fig. 4.4.

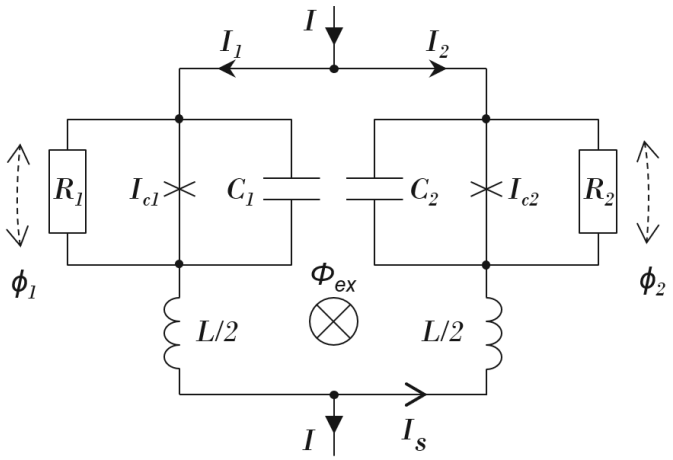

Figure 4.4: Equivalent circuit of the DC SQUID. JJs (phase differences $\phi_{1,2}$) have critical current $I_{c1,c2}$, shunted by capacitance $C_{1,2}$ and resistance $R_{1,2}$. I is the total current, split between $I_{1,2}$ for each branch, L is the loop inductance of the SQUID. I_s screening current induced by applied flux Φ_{ex}.

By using Kirchhoff's current law we can write the total current through one SQUID branch to be

$$\frac{I}{2} \pm I_s = C_i \frac{dV_i}{dt} + \frac{V_i}{R_i} + I_{ci} \sin \phi_i \quad (i = 1, 2) \tag{4.11}$$

As the voltage across the junction is described by the second Josephson relation, Eq. 3.2 we can replace the voltages in Eq. 4.11

$$\frac{I}{2} \pm I_s = \frac{\hbar}{2e} C_i \frac{d^2\phi_i}{dt^2} + \frac{\hbar}{2eR_i} \frac{d\phi_i}{dt} + I_{ci} \sin \phi_i \tag{4.12}$$

Eq. 4.12 is still missing one variable which is not present in Fig. 4.4. As type II superconductors are operating at low temperatures we need to consider the contribution from the thermal noise I_{ni}.

$$\frac{I}{2} \pm I_s = \frac{\hbar}{2e} C_i \frac{d^2\phi_i}{dt^2} + \frac{\hbar}{2eR} \frac{d\phi_i}{dt} + I_{ci} \sin \phi_i + I_{ni} \tag{4.13}$$

For the simplification we will assume that JJs are identical thus the critical current, capacitance and resistance are the same for both JJs. Eq. 4.14 shows the complete analytical model of the DC SQUID where the junctions are assumed to be identical.

$$\frac{I}{2} \pm I_s = \frac{\hbar}{2e} C \frac{d^2\phi_i}{dt^2} + \frac{\hbar}{2eR} \frac{d\phi_i}{dt} + I_c \sin \phi_i + I_{ni} \tag{4.14}$$

To analyse the Eq. 4.14 one has to consider the total current to be $I = I_1 + I_2$, phase difference as in Eq. 4.9 and use computer simulations or approximations. For this thesis we will use an approximation, where junction capacitance is zero and $\beta_L \ll 0$. Before moving further let us

also explain another parameter which was already introduced in the section 3.2. β_c, so-called *Stewart-McCumber* parameter (also called damping parameter)

$$\beta_c = \frac{2\pi I_c R^2 C}{\Phi_0} \tag{4.15}$$

The value of β_c similarly to single JJ, sets the limit for the hysteretic ($\beta_c > 0.7$) and nonhysteretic ($\beta_c \leq 0.7$) IV characteristics of the SQUID. If the junction capacitance is $\beta_L \ll 0$, neglecting thermal noise and using trigonometrical sum to product identity we rewrite Eq. 4.14

$$I = I_1 + I_2 = \frac{\hbar}{2eR}\frac{(d\phi_1 + d\phi_2)}{dt} + 2I_c \cos\left(\frac{\phi_1 - \phi_2}{2}\right)\sin\left(\frac{\phi_1 + \phi_2}{2}\right) \tag{4.16}$$

Eq. 4.9 due to the $\beta_L \ll 0$ reduces to the simpler form of $\phi_2 = \phi_1 + 2\pi\Phi_{ex}/\Phi_0$ and by defining new phase $\phi = \phi_1 + \pi\Phi_{ex}/\Phi_0$ (Φ_{ex} - constant) we get

$$I = \frac{\hbar}{eR}\frac{d\phi_1}{dt} + 2I_c \cos\left(\frac{\pi\Phi_{ex}}{\Phi_0}\right)\sin\left(\phi_1 + \frac{\pi\Phi_{ex}}{\Phi_0}\right) \tag{4.17}$$

We see that the $\cos$ part is nothing else than Eq. 4.6 and taking the time derivative of $\phi = \phi_1 + \pi\Phi_{ex}/\Phi_0$ we can write

$$I = \frac{\hbar}{eR}\frac{d\phi}{dt} + I(\Phi_{ex})\sin\phi \tag{4.18}$$

Finally, we rearrange Eq. 4.18 and using again the second Josephson relation (Eq. 3.2) we get

$$V = R(I - I(\Phi_{ex})\sin\phi) \tag{4.19}$$

Integrating V over the Josephson oscillation period τ gives the average voltage $\langle V\rangle$ across the SQUID

$$\langle V\rangle \approx \frac{RI}{2}\left[1 - \left(\frac{2I_c}{I}\cos\frac{\pi\Phi_{ex}}{\Phi_0}\right)^2\right]^{1/2} \tag{4.20}$$

By analysing Eq. 4.20 one can deduce few useful approximations for evaluation of SQUID characteristics. Comparing the Eq. 4.20 to the 4.6 we can see that also SQUID averaged voltage response at selected current value I is rectified sinusoid. For instance, if we assume operating point at $I = 2I_c$ (practical point of operation)

$$\langle V\rangle \approx \ RI_c\left[1 - \left(\cos\frac{\pi\Phi_{ex}}{\Phi_0}\right)^2\right]^{1/2} \tag{4.21}$$

this is also understood as flux response at selected biasing current (flux-voltage characteristics - ΦV- characteristics). For the current-voltage characteristics (IV- characteristics) we lock the applied flux Φ_{ex} and change the current. Another important parameter is the gain of the SQUID defined at the fixed current

$$\left(\frac{dV}{d\Phi_{ex}}\right)_{I=2I_c} = \frac{RI_c\pi}{\Phi_o}\left(\frac{\sin\left(\frac{\pi\Phi_{ex}}{\Phi_0}\right)\cos\left(\frac{\pi\Phi_{ex}}{\Phi_0}\right)}{\sqrt{1 - \cos\left(\frac{\pi\Phi_{ex}}{\Phi_0}\right)}}\right) \tag{4.22}$$

To find the maximum value of Φ_{ex} we maximize the part of Eq. 4.22 which is inside the brackets and the results are shown in the Fig. 4.5

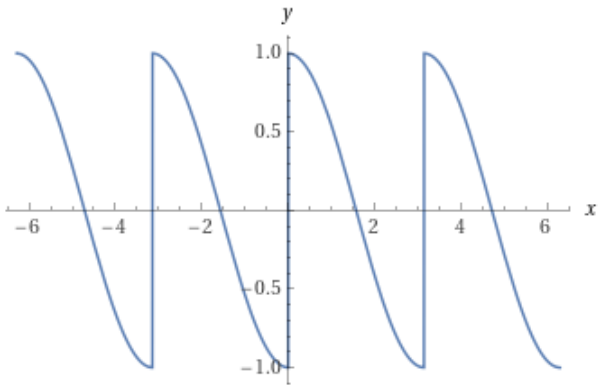

Figure 4.5: x-axis represents the value of $\pi\Phi_{ex}/\Phi_0$ and the y-axis the result of the equation part in the brackets for the Eq. 4.22.

We see in the Fig. 4.5 that this is a periodic function with the periodicity π. This means that $\Phi_{ex} = \Phi_0$ for the gain to be

$$\left(\frac{dV}{d\Phi_{ex}}\right)_{I=2I_c} = \frac{RI_c\pi}{\Phi_o} = \pi\frac{\Delta V}{\Phi_0} \tag{4.23}$$

Eq. 4.23, where ΔV is voltage modulation, is the gain approximation for the rectified sinusoid of the average voltage response in the case where the SQUID inductance is negligible $\beta_L \ll 0$ and JJ capacitance is zero. Before moving forward with the next subsections, describing the characteristics of the real SQUID devices, let us have a small summary. As we have seen, β_L (Eq. 4.10) and β_c (Eq. 4.15) will determine the design parameters such as critical current I_c and shunt resistance R while knowing the JJ capacitance and the inductance of the SQUID. Once these parameters are known one can estimate critical current density. In reality, both β_L and β_c are never zero, thus as suggested by [8] the optimal energy resolution and nonhysteretic response of the SQUID is achieved if $\beta_L \sim 1$ and $\beta_c \leq 0.7$. In addition, the gain in Eq. 4.23 is in reality very dependent on β_c choice and the gain has to be determined locally, preferably at the linear part of the SQUID voltage response.

4.2.2 Current voltage characteristics

Fig. 4.6 represents IV characteristics of a SQUID array, with the magnetic flux being generated by so-called setpoint coil, measured in liquid helium. IV plot is acquired by sweeping the bias current of the SQUID, changing the DC current of the flux generating coil (coil) and the average voltage is read out using differential low noise amplifier (LNA). This SQUID has 4 parallel array chains, with 40 SQUID cells in series in each chain. Fig. 4.6 x-axis shows the bias current through the SQUID and y-axis is the voltage response across the SQUID cell. By rough eyeball estimate, we can see that the higher critical current value $I_{c,HIGH} = 100\ \mu A$ and lower one $I_{c,LOW} = 55\ \mu A$. Symmetrical shapes on both sides of y-axis indicate that both JJs critical currents are similar among the SQUID cells, as dissimilar critical currents would lead to so-called bias-to-flux coupling. Considering the 4x40 array, we can deduce the critical current of a single JJ. Based on the general *Ohms law*, in parallel currents divide equally (if the resistance is similar) and we would get $12.5\ \mu A$ per JJ. For $I_{c,HIGH}$ and $I_{c,LOW}$ we get the critical current modulation of

SQUID $\Delta I_c = 45\ \mu A$. This current modulation is the effect caused due to the screening currents induced by the applied magnetic described by Eq. 4.9, being the highest at $(n+1/2)\Phi_0$ and zero at $n\Phi_0$ (Fig. 2.2).

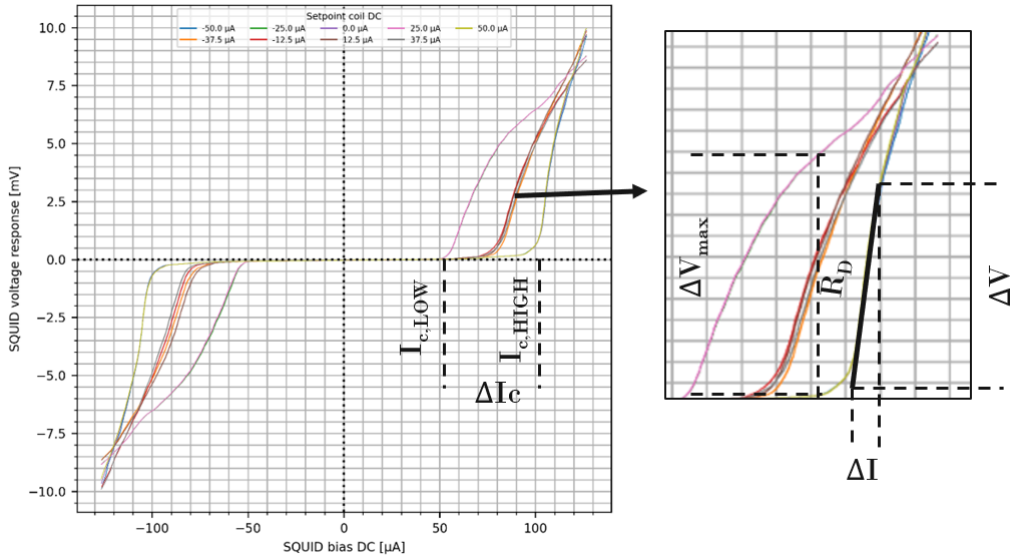

Figure 4.6: 4x40 SQUID array IV characteristics [see Appendix 3].

Another parameter to extract from the IV characteristics is dynamic resistance R_D. R_D becomes important in the energy resolution of the SQUID, in case the energy resolution is limited by the readout amplifier noise rather than by the SQUID itself. Shown by [10], when the optimal source impedance of the preamplifier R_{opt} is equal to the SQUIDs R_D, the preamplifiers contribution to the energy resolution is minimized. In similar way as the Eq. 4.23 was derived, one can also derive R_D by taking the derivative of Eq. 4.20, but this time $R_D = dV/dI$. The result is R_D approximation

$$R_D = \frac{R}{\sqrt{2}} \tag{4.24}$$

$I_{c,HIGH}$ and $I_{c,LOW}$ dynamic resistance can be estimated from the IV characteristic as $R_D \approx \Delta V/\Delta I$ (Fig. 4.6), taken from the most linear part of the slope. Respectively, we get $R_{D,HIGH} = 500\ \Omega$ and $R_{D,LOW} = 250\ \Omega$. Using the Eq. 4.24, we get resistances $R_{HIGH} \approx 707\Omega$ and $R_{LOW} \approx 354\Omega$. Now it is important to remember that we are analyzing the characteristics of the SQUID, with 4x40 array. Using the Ohms law we could try deducing the single SQUID cell shunt resistance. One can deduce the total resistance, for a single row of 40 SQUID in series chain, to be $R_{row} = 2800\Omega$, thus single SQUID would have a resistance of 70Ω. This is just an approximation and as the Eq. 4.24 is only a special case derived for the simplified RCSJ, where $\beta_c \approx 0$, $\beta_L \approx 0$, $I = 2I_c$ and $\Phi_{ex} = \Phi_0/4$. However, there is another way to estimate R_D.

One relation, which yet has not been discussed is the difference between the shunt resistance, normal state resistance and dynamic resistance. To understand the difference, lets analyze the IV characteristics of another SQUID array (Fig. 4.7). In Fig. 4.7, line passing 0 point of the both axis, shows the normal state resistance R_n of the SQUID. This in practise is the actual shunt resistance of the JJ and also corresponds to normal state resistance.

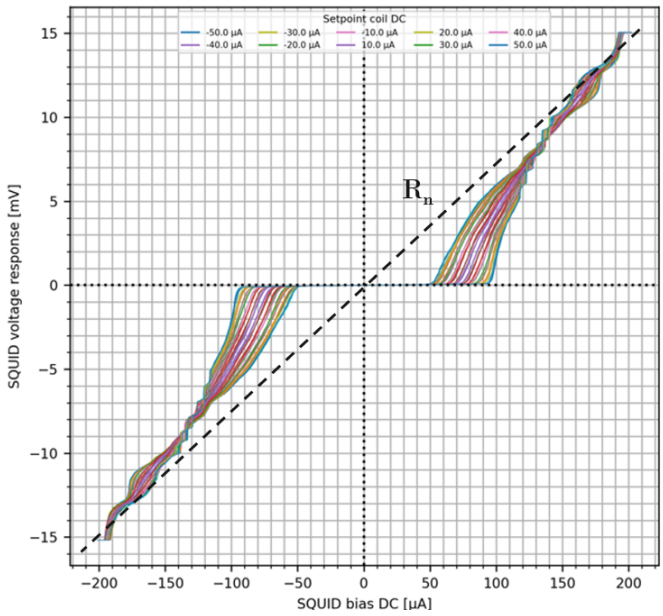

Figure 4.7: 4x40 SQUID array IV characteristics, with the black dashed line showing the normal state resistance R_n [see Appendix 4].

To understand R_D one has to remember that in the actual shunted JJ both shunt current and Cooper pair tunneling coexists in parallel. On the other hand, in an unshunted JJ it is the R_n of the quasiparticle branch that is seen at high bias currents.

Lastly, voltage modulation depth ΔV (Fig. 4.6) can be understood as a parameter to set the dynamic operation range of the SQUID. In addition, the maximum modulation ΔV_{max} is proportional to the maximum gain $dV_{max}/d\Phi_{ex}$. Maximum modulation can be read directly from the both IV- and ΦV- characteristics plots. For reading the maximum modulation from IV plot, one has to find maximum difference between $I_{c,HIGH}$ and $I_{c,LOW}$ curves - ideally the starting point is taken where $I_{c,HIGH}$ curve is switching from superconducting mode to the finite voltage mode. From Fig. 4.6, we find maximum modulation being $\Delta V_{max} = 6\ mV$, at $I_{c,HIGH} = 100\ \mu A$.

4.2.3 Flux voltage characteristics

Fig. 4.8 shows SQUID ΦV characteristics (also called flux response) plot of the same SQUID as in Fig. 4.6. ΦV characteristics are acquired by sweeping the current to one of the flux-generating coils and stepping DC for the SQUID bias current. Here x-axis shows the current injected into the coil. As mentioned in the previous subsection, the maximum modulation was estimated from the $I_{c,HIGH} = \pm 100\ \mu A$, which corresponds to the dark blue curve of the positive and orange curve of the negative side of the flux response plot. Both of the curves show the maximum modulation of $|\ \Delta V_{max}\ | \approx 5.8\ mV$, which is close to what we estimated from the IV characteristics. The small difference is caused due to the small number of the steps chosen for stepping the SQUID biasing current. The periodicity of rectified sinusoidal response along x-axis, is the periodic response of flux quantum of $50\ \mu A/\Phi_0$ (also referred to as inverse mutual inductance M^{-1}).

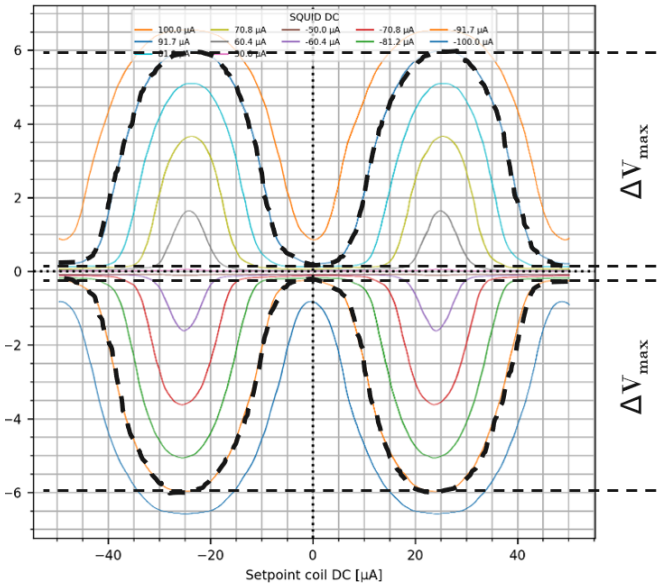

Figure 4.8: ΦV characteristics of the same SQUID as in Fig. 4.6. Y-axis SQUID voltage response in mV.

Let us analyse a bit more the SQUID flux response characteristics for the gain $dV/d\Phi$. There is at least two ways to estimate the gain of the SQUID. An easy one, is to use so-called triangular approximation where the gain is equal to a slope of $dV/d\Phi \approx 2\Delta V/\Phi_0$. For Fig. 4.9 we would estimate maximum gain as $dV_{max}/d\Phi \approx 2\Delta V_{max}/\Phi_0 = 2 * 5.8 = 11.6\ mV/\Phi_0$.

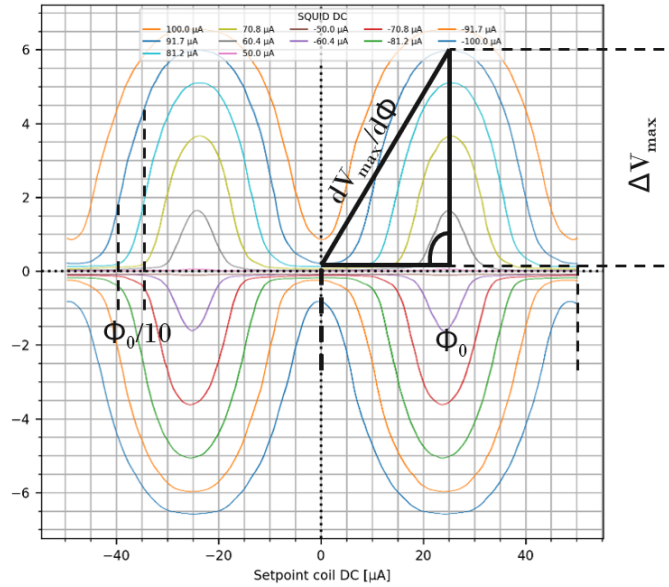

Figure 4.9: ΦV characteristics of the same SQUID as in Fig. 4.6. Y-axis SQUID voltage response in mV.

On the other side, we can also estimate the gain by choosing close to the linear slope of the rectified sinusoidal, flux response signal, for instance, $1/10^{th}$ or $1/20^{th}$ of Φ_0. By choosing $\Phi_0/10$, being 5 μA on the x-axis we get $\Delta V \approx 2.5\ mV$. That would result in the gain of $dV_{max}/d\Phi \approx 25\ mV/\Phi_0$, twice higher than in the triangular approximation. Here we have to

consider that SQUID flux response is non-linear and the gain found with the last method would only count for the region of operation at the so-called *sensitive operation point* of $\Phi_0/10$. One more way to find the gain is to use Eq. 4.23, derived for rectified sinusoid response of the average voltage, $dV_{max}/d\Phi = \pi\Delta V_{max}/\Phi_0 = \pi * 5.8 = 18.2\ mV/\Phi_0$.

Finally, now when we have seen the gain, we can calculate trans-resistance by dividing the gain with inverse mutual, resulting in the value describing relation between injected current into the coil and resulting voltage response across the SQUID, with the units V/A. For the SQUID in Fig. 4.9, we consider $M^{-1} = 50\mu A/\Phi_0$ and the gain $18.2\ mV/\Phi_0$, which give the trans-resistance $R_T = 364V/A$. In addition, to the analytical analysis of the SQUID plots, one has to also pay attention on the asymmetries and unusual shapes, such as, peaks, flat plateaus or excess ripple present in the SQUID response.

Chapter 5

Irregularities in electrical characteristics

5.1 Changes in shunt resistance

Previously introduced two key parameters β_c (Eq. 4.15) and modulation parameter β_L (Eq. 4.10) play an important role in the analysis of the SQUID characteristics. As a value, resistance should be such that $\beta_c < 0.7$ for nonhysteretic response of SQUID. One way to analyze this balance is to compare the magnitudes of the values present in β_c. For instance, $\Phi_0 \approx 2.07 \cdot 10^{-15}\ Wb$, $I_c = 10\ \mu A$ per junction, JJ capacitance $C_j = 75\ fF$ and shunt resistors are nominally $17.5\ \Omega$ - design values for SQUID cell. In addition, for the high quality SIS unshunted JJ, resistance is approximately $R_n e^{\Delta/k_B T}$ for $V < V_g$ [5]. Thus, if we do not have a smaller resistance in parallel with the junction own resistance then β_c will go to infinity (underdamped junction $\beta_c > 0.7$) and SQUID will experience hysteresis [1]. Fig. 5.1 shows IV response of the SQUID with the hysteresis in the response.

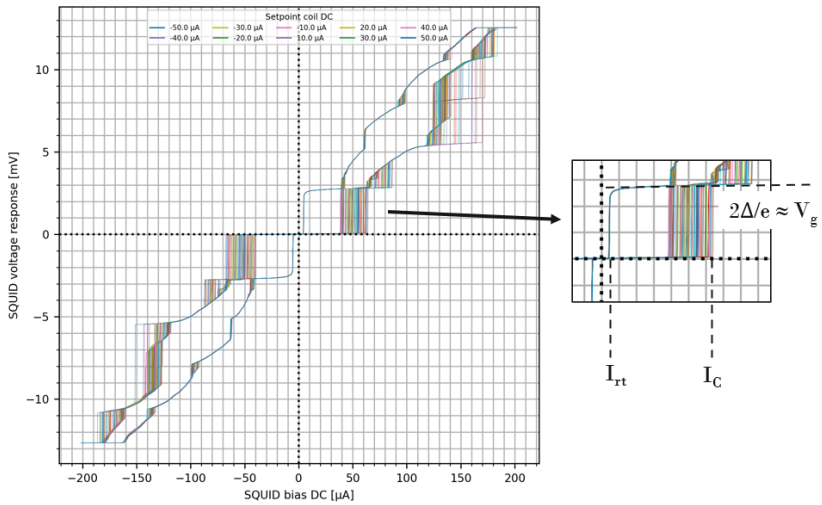

Figure 5.1: 4x40 SQUID array IV characteristics showing hysteresis in the response [see Appendix 5].

[1] Another way of explaining β_c is in the relation to so-called *tilted washboard model*. In that model capacitance represents the mass of the particle in the washboard potential, whose tilt is change using the current I.

Seen in the Fig. 5.1, at critical current, there is a sharp jump from superconducting to the finite voltage state, this finite voltage shown as V_g is as symbol suggests nothing else than a gap voltage of the JJ. JJ of the SQUID in Fig. 5.1 is $Nb/Al/AlO_x/Nb$ type, as discussed in the section 3.1, the gap value for this type of JJ is $2\Delta = 2.8mV$. In addition, one can see that also the ΔI exists thus flux coupling takes place. Once SQUID is in the finite voltage state the normal state resistance at higher currents is the actual JJ normal state resistance. Once the current through the SQUID is reduced, the switching back to the superconducting state does not occur at I_c, but at so-called retrapping current I_{rt} [2].

One has to be careful before stating exactly if the shunt resistor is missing or has broken connection. For instance, Fig. 5.2(right) shows a response of a different device as in Fig. 5.2(left), but finite voltage state can be seen. Even if the shunt is present, it should be considered that also too high critical current or too high capacitance value may introduce hysteresis. For instance, if during the fabrication JJ size gets accidentally enlarged, causing the critical current to increase, it can cause also hysteretic response.

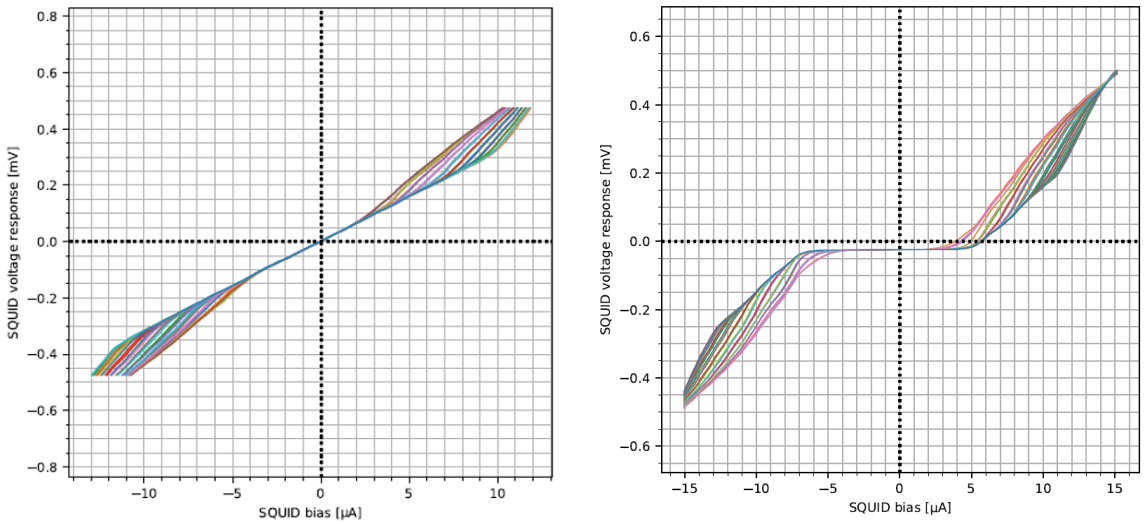

Figure 5.2: 1x2 SQUID array IV characteristics. Indicating at least one of the SQUID cells with damaged JJ structures [see Appendix 6] and another one has different critical currents among individual SQUID cells [see Appendix 7]

Fig. 5.2(left) is an example of a response where the shunt is present, linear slope would give an estimate of $\approx 15\ \Omega$ per JJ (reasonable value to expect), but no superconducting state is seen in the response. This indicates that one of the SQUIDs, in 1x2 SQUID array, has both JJs broken, thus the resistive line. As a result, the characteristics of the second, functioning SQUID, are added on top of the broken one. The same phenomena applies for the larger arrays, even if the rest of the SQUID cells are superconducting, the higher voltage overrides the results. Fig. 5.2(right) may be misleading as one may consider the "sliced" IV-characteristics being an artifact of the damaged shunt resistance, however, the issue may be different critical current among JJs or broken JJs.

[2] Retrapping current is different than the critical current because of the quasiparticles having momentum (compared to the inertia of the moving mass) and the energy of that momentum has to be dissipated.

To end this section, let us still show the contribution of the SQUID resistance to the β_c. Fig. 5.3 shows *LTspice* result of the simulations for different resistance values.

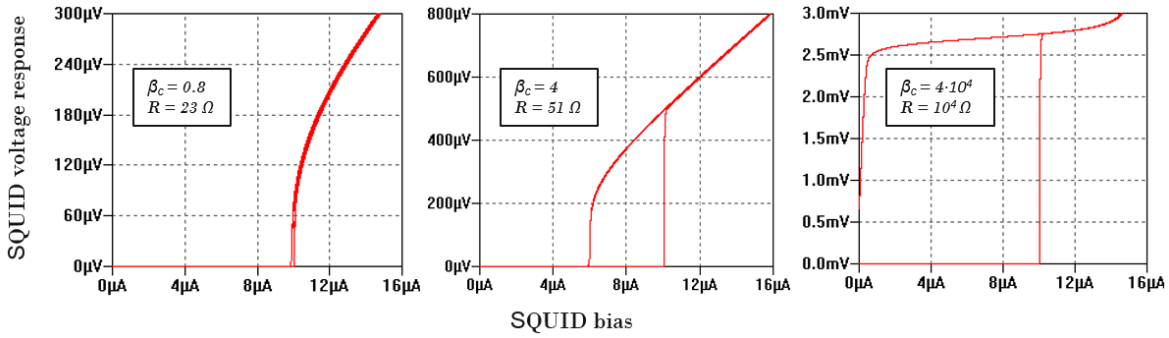

Figure 5.3: *LTspice* simulation for SQUID IV characteristics at different resistance values. The model included under Appendix 8.

Simulation results in Fig. 5.3 indeed reflect the expected behaviour of the SQUID, with different resistance values. One interesting result is that by changing the resistance $23 \rightarrow 51\ \Omega$, the change is enough to have SQUID become hysteretic.

5.2 Capacitive loading

So far we have not considered the fact that due to the complex designs and geometries used to fabricate SQUIDs, different parasitics have to be considered in the calculations of β_c and β_L. For instance, JJ can have in addition to own junction capacitance also indirect capacitive coupling to the flux generating coil(s) or connection to the external electronic circuit introducing capacitive loading or capacitive feedback. It has been shown that high frequency oscillation is produced by the flux generating coil resonance, in the case of the capacitive coupling between the flux generating coil and SQUID loop [29]. One of the results is shown in the Fig. 5.4(right), where the parasitic capacitance of $3\ pF$ introduces distortions (so-called plateaus) in ΦV characteristics.

.

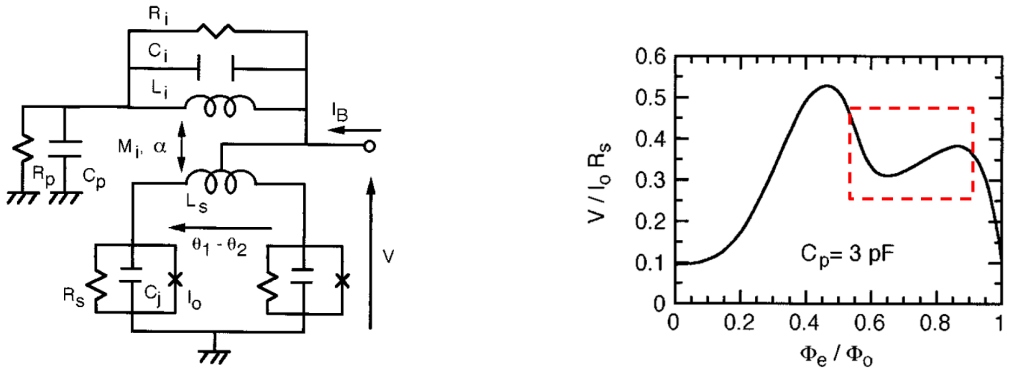

Figure 5.4: RCSJ model of the coupled SQUID taking into account the input coil resonance and the parasitic capacitance (left) [3]. Distortion of ΦV characteristics due to the input coil resonance and the parasitic capacitance marked red (right). [29]

In addition, to the applied DC flux of the coil (Φ_{ex}), the feedback mechanism creates additional AC flux through the resonating circuit formed by the parasitic capacitance C_p. This flux will add on top of the, user-controlled flux Φ_{ex}. Fig. 5.4(right) shows the splitting in the SQUIDs flux response due to the resonance of the flux generated by the coil and the parasitic capacitance, induced by the capacitive feedback between the coil and the SQUID loop (Fig. 5.4(left)). As suggested by [29], the resonance frequency of the coil can be for instance $\approx f_J/10$, but in general the frequency depends on the detailed SQUID dimensioning.

For the better understanding of the instabilities present, where SQUID oscillates, thus producing distortions in the ΦV- characteristics as in Fig. 5.4(right), one has to consider SQUID as an amplifier with the gain $dV/d\Phi_{ex}$. *Barkhausen stability criterion* states that if amplifier circuit has a positive feedback loop existing with the loop gain 1, circuit will sustain steady-state oscillations [4] [30]. Derived by [29], the instability condition for the circuit Fig. 5.4(left) is

$$\frac{L_i}{R_i} + \frac{L_i}{R_p} + \frac{\alpha^2 L_s}{2R_s} + (\pi C_p \Delta V M_i/\Phi_0)\sin 2\pi\Phi_{ex}/\Phi_0 < 0 \tag{5.1}$$

where R_s is SQUID normal state resistance. Eq. 5.1 has many components to contribute to the instability part, however, main contribution is set by the sign of the sine, thus giving the region for the positive feedback $\Phi_0/2 < \Phi_{ex} < \Phi_0$, which is consistent according to the Fig. 5.4. Something similar has been observed in the real SQUID characteristics (Fig. 5.5)

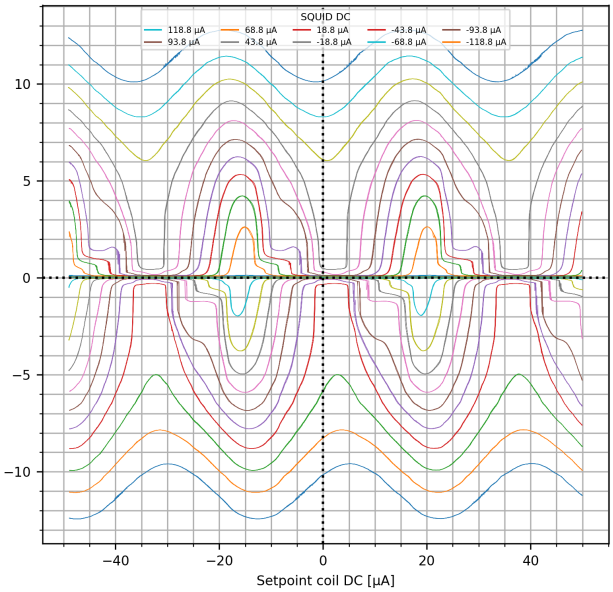

Figure 5.5: ΦV characteristics of 4x40 SQUID measured with the setup suspected to have parasitic capacitance [see Appendix 9].

[3] Resonance in the coil is achieved with coil inductance L_i and capacitance C_i, R_i is coils RF loss. Parasitic resistance and capacitance in the system are respectively R_p and C_p. Between SQUID loop (with inductance of L_s) and resonating coil we have mutual inductance M_i with the coupling constant α. Both SQUID loop and resonating coil circuits are bias with the current I_B. I_0 is the critical current of JJ and $\theta_1 - \theta_2$ is JJ phase difference.

[4] Oscillations will only occur at frequencies for which loop gain is 1 and phase-shift around loop 2π [30].

where it has been suspected that the additional capacitance, introduced by the external electronics circuit, has similar effect as in Fig. 5.4(right). To rule out the possibility of something being wrong with the SQUID internally (Fig. 5.5), a similar type of device was measured with a different setup and intentionally introduced a parasitic capacitance between SQUID loop and the coil - similar way as in Fig. 5.4(left). Results are discussed in the chapter 6.

5.3 Distribution of critical currents

Another irregularity to analyse is seen in Fig. 5.6. There one can observe so-called rounding of the IV characteristics, the switching from superconducting to finite-voltage state is not sharp. It was previously mentioned that SQUID arrays can have different size and geometries when it comes to the design and the layout on the chip and especially important being the SQUID loop and JJs. For instance, SQUID array in Fig. 5.5 has been suspected to have a mechanism to cause some sort of distribution of the critical currents in some single SQUID cells in the array, the resultant can cause rounding of the IV characteristics, as mentioned.

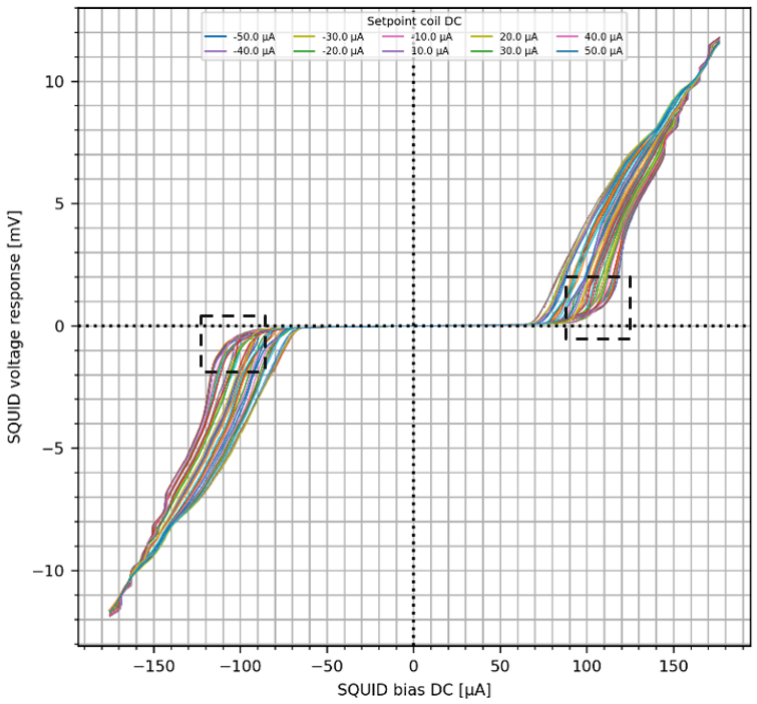

Figure 5.6: 4x40 array SQUID IV characteristics with the rounded transition from the superconducting to finite-voltage state [see Appendix 10].

One of the main disadvantages of the rounded IV characteristics can be the reduction in the maximum modulation of the SQUID. Also, if the rounding forces to choose the biasing current value close to the critical current value, which is already at finite voltage state, that may cause an additional voltage noise, reducing the resolution of the SQUID. There may be many mechanisms which can trigger this phenomenon. However, we should consider the knowledge acquired from the theoretical part of this thesis, by knowing that the critical current I_c can be affected, for instance, by temperature, external magnetic field, JJ size or the choice of β_L parameter.

Let us assume the rounding of the characteristics being caused due to the normal distribution of the critical currents among the single SQUID cells in series. Introducing probability density function $f(x)$ for the normal distribution

$$f(x) = \frac{1}{\sigma\sqrt{2\pi}} e^{-\frac{1}{2}\left(\frac{x-\mu}{\sigma}\right)^2} \tag{5.2}$$

Assigning x to be random value of critical current $I_{c,x}$ found within the range of two standard deviations 2σ of the mean value $\mu = \bar{I}_c$, we rewrite Eq. 5.2

$$f(x) = \frac{1}{\sigma\sqrt{2\pi}} e^{-\frac{1}{2}\left(\frac{I_{c,x}-\bar{I}_c}{\sigma}\right)^2} \tag{5.3}$$

It is important to mention here that x seen in $I_{c,x}$ represents the number of SQUID cells in the SQUID array of n cells. To simulate the IV response of the SQUID we use simplified model for average voltage response derived in Eq. 4.21, considering symmetrical SQUID loop with identical JJ, $\beta_L \ll 1$ and $\beta_c \approx 0$. The current through the JJs is described by Eq. 4.18 and total flux in Eq. 4.5.

$$\langle V \rangle \approx \frac{RI}{2}\left[1 - \left(\frac{2I_c}{I}\cos\frac{\pi\Phi_a}{\Phi_0}\right)^2\right]^{1/2} \tag{5.4}$$

For the case, where the SQUID voltage response does not change in the applied flux, we can rewrite Eq. 5.4

$$\langle V \rangle \approx \frac{RI}{2}\left[1 - \left(\frac{2I_{c,x}}{I}\right)^2\right]^{1/2} \tag{5.5}$$

To generate normal distribution of critical current values $I_{c,x}$ *Matlab* internal functions *makedist* and *random* are used. *Random* function is using the mean and standard deviation values set by the user to generate a random population of $I_{c,x}$ values, following the rules of the normal distribution. Results of this section will be presented in the next chapter.

5.4 Flux trapping

Before moving on to the last chapter, let us still briefly described one more irregularity discussed in the section 3.3 and observed among the SQUID arrays. It was mentioned that type II superconductors experience so-called mixed state, where the vortices generated on the surface of the superconductor are repelling the applied magnetic field, thus allowing a resistless flow of the transport current. Because niobium thin films are not well ordered, vortices will not form a regular lattice, but get preferably trapped to so-called pinning sites. Such a vortex, or a flux trap, may shift local flux seen by a randomly selected SQUID cell in the array, preventing its signal to sum constructively. This sort of flux trapping may result in decrease of the SQUID performance such as seen in the Fig. 5.7.

Fig. 5.7 shows the result of the measurement, where the SQUID was suspected to have trapped flux. From the previous measurement of similar devices, the expected critical current modulation was larger, thus a suspicion of a trapped flux was considered.

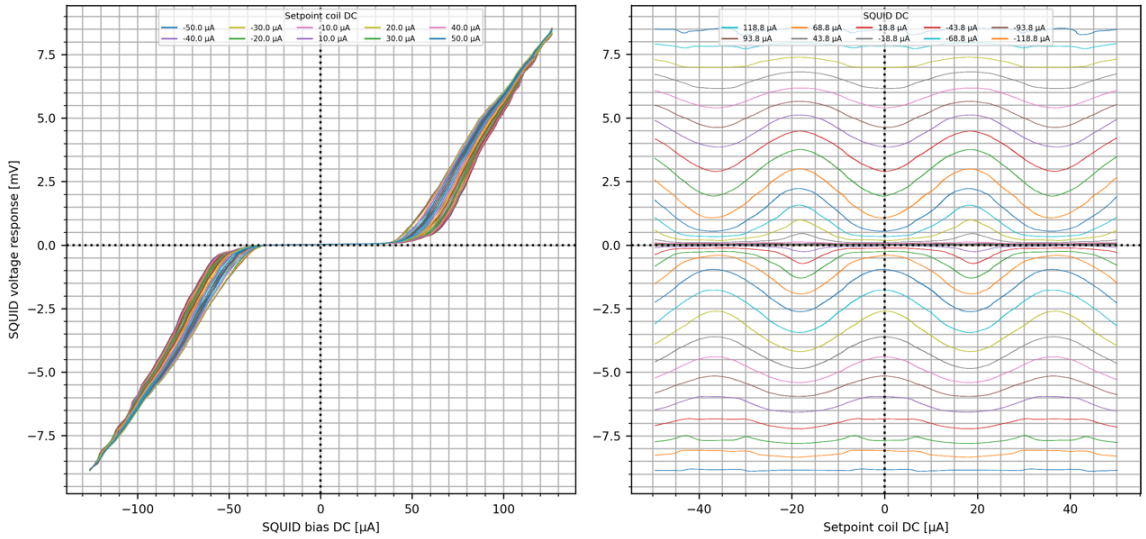

Figure 5.7: 4x40 array SQUID IV- and ΦV- characteristics with suspected trapped flux [see Appendix 11].

Fig. 5.8 shows the result after the SQUID was heated above the T_c and cooled down again to 4.2 K.

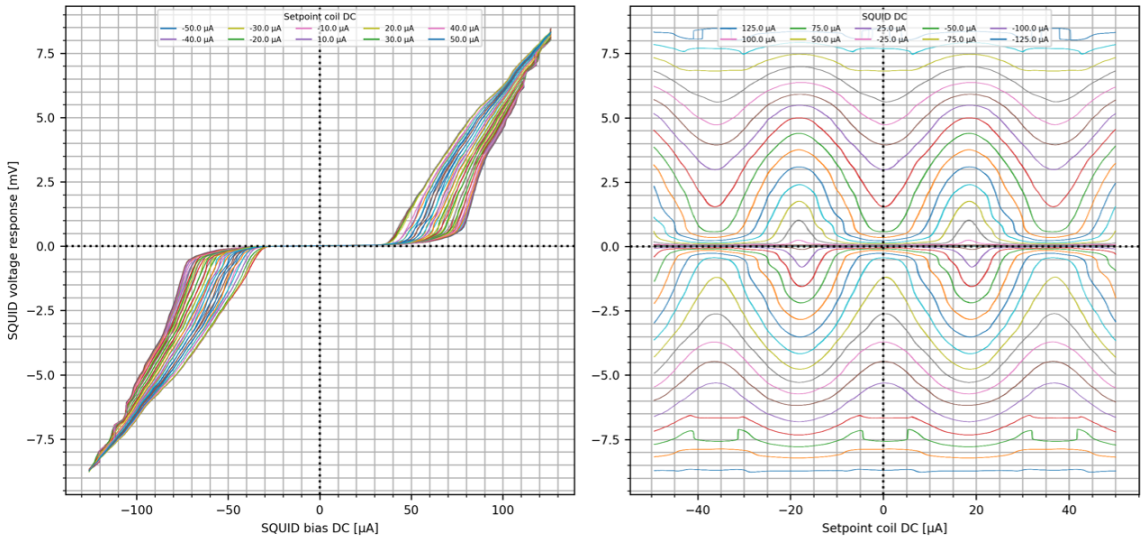

Figure 5.8: Same SQUID IV- and ΦV- characteristics, as in 5.7 after thermal cycling [see Appendix 12].

Chapter 6

Results and discussions

6.1 Simulation of the critical current distribution

Using the motivation in the section 5.3 regarding the distribution of the critical current, following results were achieved. Fig. 6.1 shows the examples of the normal distribution of critical currents, with mean value being $\bar{I}_c \approx 10\ \mu A$, standard deviation $\sigma = 1\ \mu A$.

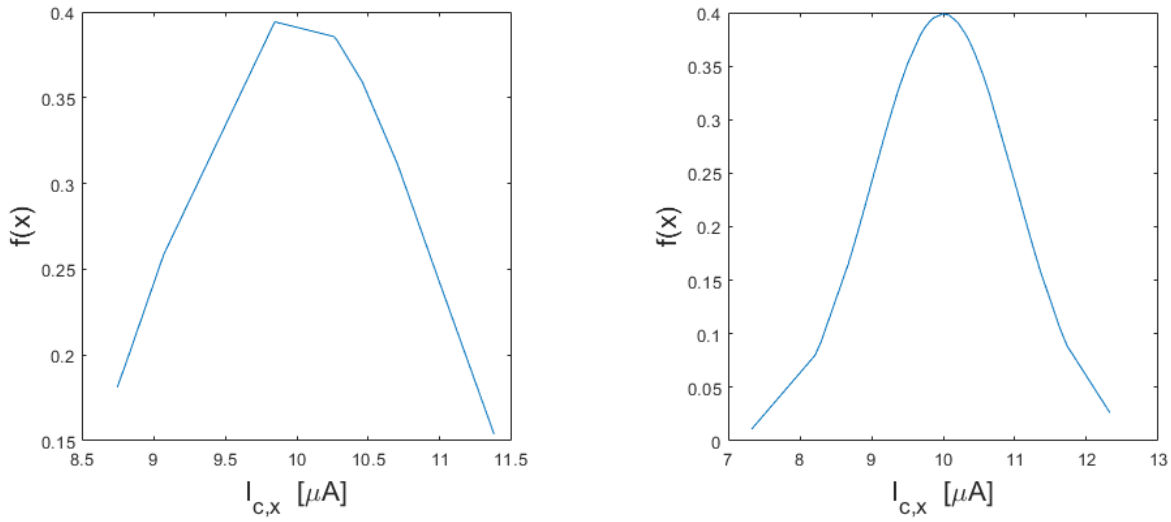

Figure 6.1: Probability density of the critical current distribution for the $n = 10$ (left) and for $n = 40$ (right). n is the number equivalent to the number of the single SQUID cells arranged in series to form a SQUID array.

Using the similar type of distributions [1], seen in Fig. 6.1, together with the Eq. 5.4, we get IV characteristics of the SQUID presented in Fig. 6.2. For the simulations, using Eq. 5.4, shunt resistor is $R = 30\ \Omega$, SQUID bias current range $I = \pm 40\ \mu A$ and number of steps 101. Comparing the results seen in Fig. 6.2 to the Fig. 5.6, the similar rounding occurs when we introduce a distribution of the critical currents. The rounding becomes more aggressive with increased standard deviation, which is intuitively reasonable as larger spectrum of different critical current values is introduced. The average voltage $\langle V \rangle$ is acquired by summing the calculated

[1] Mentioned in the previous chapter *Matlab*'s random function generator *random* is used, causing the distributions to be slightly different for each calculation round.

individual voltage values at each bias current step. This is a reasonable approach also as we assume single SQUID cells to be in series. In addition, one can spot that with higher n we get higher voltage which is in line with the fact that higher number of single cells in the SQUID array generate higher modulation. The smoothness of the rounding of the superconducting switching region to finite voltage states is proportional to the number of different critical currents.

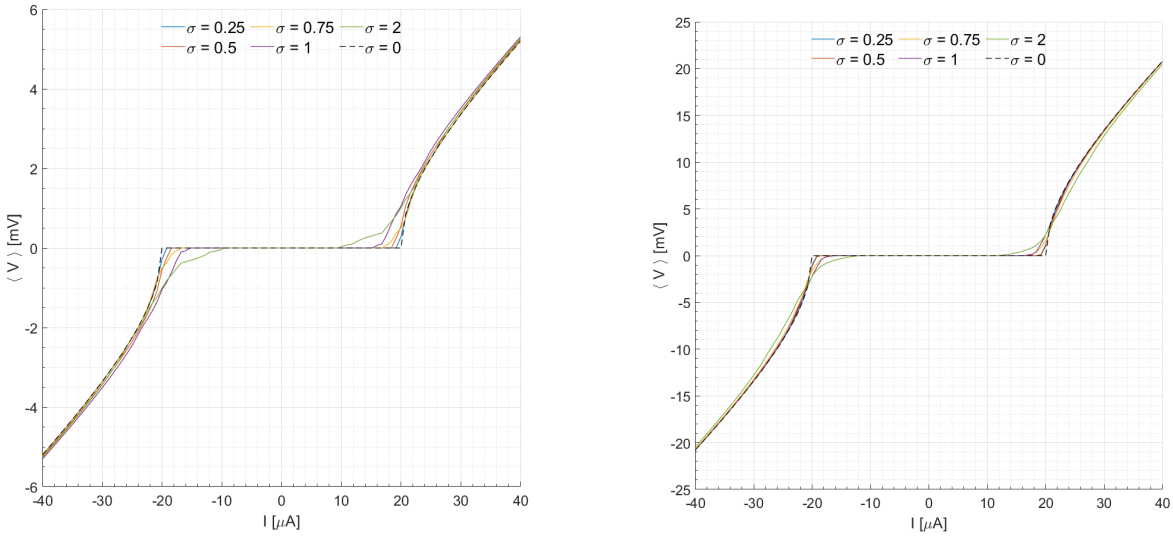

Figure 6.2: Simulated SQUID responses, with $n = 10$ (left) and $n = 40$ (right).

6.2 Measurements with the parasitic capacitance

Another motivation, introduced under the section 5.2 suggested the possibility of the instabilities in the SQUID (Fig. 5.5). To replicate similar instabilities and rule out the possibility of the suspected external circuitry capacitance, another (similar type as in Fig. 5.5) SQUID (sample) was measured with a different setup and intentional parasitic capacitance [see Appendix 13]. More accurately, sample had additional capacitor connected in between coil and SQUID loop, as schematics Fig. 5.4(left) suggests. Capacitor values of $10\ pF$ and $100\ pF$ were used in two measurements as parasitic capacitance's C_p and compared to the sample, when measured without intentional parasitic capacitance. Results of these measurements are collected in the Fig. 6.3.

Analysing Fig. 6.3 one can notice the appearance of the similar "plateaus", between $10 \rightarrow 25\ \mu A$ as seen in both Fig. 5.4(right) and Fig. 5.5. In addition, shift in the flux response peaks is present, compared to the measurement where no parasitic capacitor was soldered and a small reduction in the modulation is also seen. If the reader has not yet noticed, then for the measurements in Fig. 6.3 the excitation of the coil is happening from right to left, along the x-axis. [29] suggests that instability condition Eq. 5.1 is especially satisfied in the flux response region $3\Phi_0/4$, which is quite close to the Fig. 6.3 instability region. We can deduce that indeed the sample is experiencing instabilities caused by the positive feedback loop induced by the parasitic capacitance's [31]. However, the nature of the instabilities observed is a bit different to one in Fig. 5.4(right).

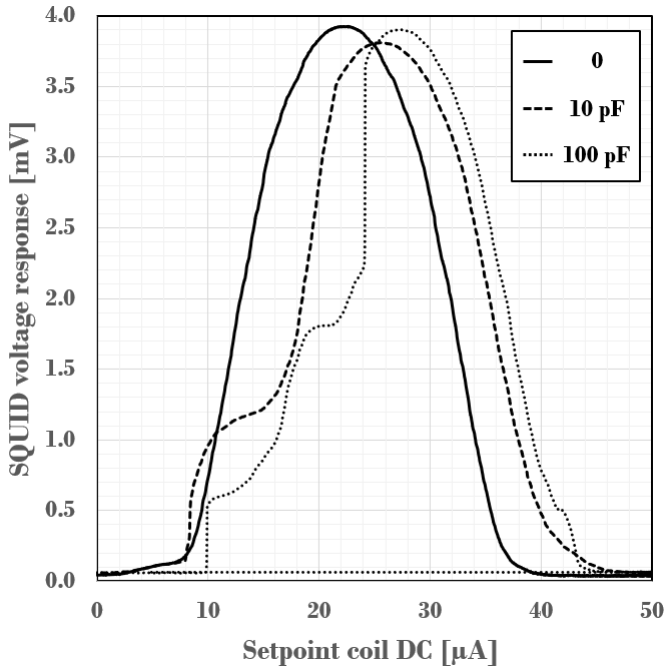

Figure 6.3: 4x40 array SQUID ΦV characteristics, measured using no parasitic capacitance (solid line), 10 pF parasitic capacitance (dashes) and 100 pF parasitic capacitance (dots). Excitation of the setpoint coil is happening from right to left, along the x-axis.

Let us write again the stability condition, suggested by [29]

$$\frac{L_i}{R_i} + \frac{L_i}{R_p} + \frac{\alpha^2 L_s}{2R_s} + (\pi C_p \Delta V M_i/\Phi_0)\sin 2\pi\Phi_{ex}/\Phi_0 < 0 \tag{6.1}$$

In addition, to the parasitic capacitance C_p, another contribution to the instability is the voltage modulation ΔV, which sets the gain. In Fig. 5.4(right), SQUID used is high temperature superconductor, which uses $SrTiO_3$ material as an insulator between coil and SQUID loop. $SrTiO_3$ relative permittivity is $\epsilon_r \approx 1800$. Sample in Fig. 6.3 is type II, low temperature superconductor and material used as insulator is SiO_2, with a lower relative permittivity $\epsilon_r \approx 3.9$. Now if we compare the voltage modulations of Fig. 6.3 and Fig. 5.4(right), the voltage modulation has approximately difference of 10. Considering lower relative permittivity and higher "negative" gain for the SQUID array, we can indeed state that the sample (Fig. 6.3) is experiencing instabilities caused by the parasitic capacitance.

6.3 Possible improvements

Irregularities described in the previous chapter still may be lacking complete explanations to understand the root cause of the distortions. For instance, the issues with the shunt resistance may be verified by examining the SQUID using different techniques of microscopy such as focused ion beam (FIB) technique together with scanning electron microscope (SEM). To study the flux trapping phenomenon a more complex approach should be used. For instance, introduction of external controlled flux and quantitatively analyse the critical values of the magnetic field needed to induce flux trapping. In addition, one has to analyze the heat amount needed to allow sample

heating above T_c, without causing permanent damages to the SQUID structures.

One of the main results as we saw was to be able to replicate the rounded IV characteristics observed in the SQUID arrays. The approach used, was more of a direct way to explain the rounding. However, SQUID is a nonlinear device and while modulation parameter β_L can be chosen carefully during the designing step, considering the relation between SQUID inductance and critical current, the derivation of Eq. 4.21, neglected both β_L and β_c. For more accurate/realistic results more complicated model should be used, which could at least include β_L parameter, thus introducing critical current modulation in the simulations. Another way to see the effect of the critical current distribution among individual SQUID cell is to study in addition to IV characteristics also ΦV- characteristics. For instance, it has been shown by [32] that asymmetric JJ due to the variations in the critical current and shunt resistances can produce shifts and voltage modulation decrease in ΦV- characteristics of parallel SQUID array. Fig. 6.4(a) shows that if shunt resistances are all the same then due to the asymmetry in the critical currents the shifting in the flux response happens and decrease in the modulation takes place - $\alpha = 0$ means critical currents are equal. Similar behaviour is observed when critical current is constant among SQUID cells, but resistances vary (Fig. 6.4(b)), however, the effect is weaker then with the variation of the critical currents.

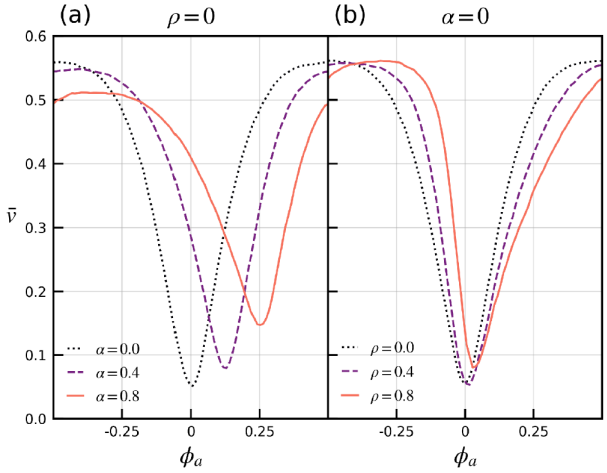

Figure 6.4: Normalized voltage versus normalized applied flux of a 1D parallel SQUID array with Np = 10 and asymmetric junctions. $\bar{\nu}$ is normalized time-averaged voltage, α is normalized degree of asymmetry of the junction's critical currents and ρ is normalized degree of asymmetry of the junction's shunt resistances [32].

6.3.1 Design features

Last but not least, one way to analyse and understand the effect of the changes in shunt resistance, loop inductance or both parasitic inductance and capacitance, is to intentionally fabricate devices with the known design "flaws". For instance, Fig. 5.2(right) already showed a potential distribution of the critical current(s) in the small array of the series SQUID cells. Confirming these intentional design errors by measuring smaller arrays or even single SQUID cells would ease up the complexity needed to be considered for the large, SQUID arrays. However, study of large, SQUID

arrays with the more sophisticated approach than in this thesis is needed to also understand the coherence between the different SQUID cells and cell arrays. Coherence between single SQUID cells in the array plays an important role in the voltage response of the whole array. For instance, as suggested by [33] for a series array of 100 SQUIDs, due to the variations in critical currents and trapped flux, localised gradient fields caused by the flux generating coils or some combinations of these, SQUID array will have a different ΦV characteristics than for single SQUID, Fig. 6.5. In addition, voltage modulation dropped by $20\ \%$ when the applied flux was increased to $10\ \Phi_0$. As explained by [33] the change observed was attributed to small differences in the mutual inductance among the individual SQUIDs, causing each SQUID to operate at different flux periodicity.

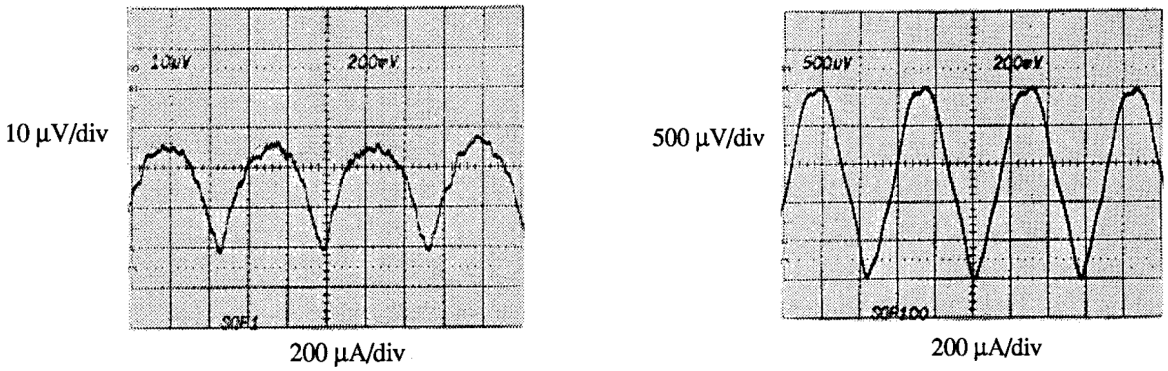

Figure 6.5: ΦV- characteristics of the single SQUID (right) and a series array of 100 (left) of a similar design as in (left) [33].

Chapter 7

Conclusion

Cryogenic detector systems require intermediate power amplifiers, with a large enough output signal to overcome thermal noise of $T = 300\ K$ ordinary electronics. Such intermediate amplifiers are needed eg. in the X-ray detector array system targeted for the X-IFU instrument onboard the ATHENA mission [9]. A DC SQUID is a cryogenic amplifier with many convenient properties, but its typical signal level is proportional to the $T = 3\ K$ thermal noise, i.e. 100 times lower than typical room-temperature signal levels. One way to increase SQUID signal levels is to arrange many DC SQUIDs into an array where the individual SQUID signals add coherently.

Many mechanisms may spoil the coherence, including: (i) statistically distributed rather than single-valued parameters of the constituent JJs, in particular their critical currents; (ii) at an extreme case of the statistical distribution, a failed single junction, or a failed single SQUID cell, where its both JJs fail; and (iii) flux trapping which may create local flux shifts that spoil the coherence. Additionally (iv) large-gain, large-bandwidth amplifiers such as SQUID arrays may become unstable due to parasitic feedback effects, whether internal in the SQUID chip or external due to cryogenic wiring or other aspects of the experimental setup.

This thesis work regards observation of the above degradatory mechanisms, by features that can be recognized in the measured IV- and ΦV- characteristics of particular SQUID array samples. at liquid helium temperature. Recognition of the presence of a degratory mechanism on a particular sample is a basis on whether the sample can be delivered to a customer, or whether it should be rejected. Additionally, occurrence frequency and severity of the observed non-idealities provide valuable feedback about the SQUID fabrication and bottlenecks of the fabrication process.

Acknowledgements

This thesis has been written in collaboration with my current employer VTT, where I work as a Research Assistant in the Quantum Sensors team and my home university Tallinn University of Technology. The thesis work carried out has been financed by VTT and the European Space Agency ESA. Mikko Kiviranta (Principal Scientist) has been an excellent supervisor with the ability to guide me towards the correct direction and always being ready to provide a precise answer to any question asked. Under his guidance I have gotten valuable insight into the SQUIDs, the general field of low temperature physics and how the research should be carried out. He has also provided the $LTspice$ model used for the simulations. Professor Mihhail Klopov has provided me with the needed help from the university side, such as, proof-reading, following general guidelines, commenting my work and he has been very efficient in providing me the feedback.

I want to thank D.Sc. Eija Tuominen, who provided support throughout the whole thesis writing process. Her valuable time for proof-reading, commenting the written work and finding flexible working conditions in parallel with thesis writing. I would like to thank Ph.D Erik Jellyman for the proof-reading, commenting and his ideas on how to improve the structure of the thesis. I would also like to thank the members of both VTT research teams, Quantum Sensors and Quantum Hardware, to have shown their interest into my research and thesis.

Last but not least, I want to express my gratitude towards my family who have always supported me and my studies. Also, to both of my cats, who have kept the paperwork in order.

References

[1] L. Gottardi et al. “Sensitivity of the spherical gravitational wave detector MiniGRAIL operating at 5 K”. In: *Phys. Rev. D* 76.10 (2007).

[2] M. Hämäläinen et al. “Magnetoencephalography—theory, instrumentation, and applications to noninvasive studies of the working human brain”. In: *Rev. Mod. Phys.* 65.2 (1993).

[3] J. N. Ullom and D. A. Bennett. “Review of superconducting transition-edge sensors for x-ray and gamma-ray spectroscopy”. In: *Supercond. Sci. Technol.* 28 (2015), p. 36.

[4] D. van Delft. “Little cup of helium, big science”. In: *Physics Today* 61.3 (2008), pp. 36–42.

[5] M. Tinkham. *Introduction to Superconductivity, 2nd ed.* Dover Publications Inc., 2004.

[6] E. Jellyman. *Investigations into the vortex lattice of Ni-chalcogenide and Fe-arsenide super-conductors, using small-angle neutron scattering.* PhD thesis, University of Birmingham, 2018.

[7] T. van Duzer and C. W. Turner. *Principles of Superconductive Devices and Circuits, 2nd ed.* Prentice Hall-PTR, 1999.

[8] J. Clarke and A. I. Braginski (eds.) *The SQUID handbook. Vol. 1. Fundamentals and technology of SQUIDs and SQUID systems.* WILEY-VCH Verlag GmbH Co. KGaA, Weinheim, 2004, pp. 170–217.

[9] D. Barret et al. “The Athena X-ray Integral Field Unit: a consolidated design for the system requirement review of the preliminary definition phase”. In: *Experimental Astronomy* 55 (2023), pp. 373–426.

[10] T. Ryhänen et al. “SQUID magnetometers for low-frequency applications”. In: *J. Low Temp. Phys.* 76.5/6 (1989), pp. 287–386.

[11] C. D. Tesche and J. Clarke. “dc SQUID: Noise and optimization”. In: *J. Low Temp. Phys.* 29 (1977), pp. 301–331.

[12] *P451/551 Lab: Superconducting Quantum Interference Devices (SQUIDs)*. 2014. URL: `https://api.semanticscholar.org/CorpusID:198928094` (visited on 12/28/2023).

[13] *This Month in Physics History, January 19, 1894: James Dewar produces solid air.* 2012. URL: `https://www.aps.org/publications/apsnews/201201/physicshistory.cfm` (visited on 12/28/2023).

[14] C. Kittel. *Introduction to Solid State Physics*. John Wiley & Sons, Inc., 2005, pp. 259–296.

[15] *Johnson–Nyquist noise*. URL: https://en.wikipedia.org/wiki/Johnson-Nyquist_noise (visited on 12/28/2023).

[16] R. K. Loide. *Kaasaegne Füüsika II, Lecture notes*. Tallinna Tehnikaülikool, 2014.

[17] N. H. Balshaw. *Practical cryogenics. And introduction to laboratory cryogenics*. Oxford Instruments, Whitney (United Kingdom). Scientific Research Div, 1996, p. 36.

[18] V. Ambegaokar and A. Baratoff. "Tunneling Between Superconductors". In: *Phys. Rev. Lett.* 10.11 (1963).

[19] Y. Lu P. N. Butcher. *Superconductivity: From Basic Physics to the Latest Developments*. World Scientific, 1995, pp. 45–78.

[20] L. Grönberg et al. "Fabrication Process for RSFQ/Qubit Systems". In: *IEEE Trans. on Appl. Supercond.* 17.2 (2007), pp. 952–954.

[21] D. E. McCumber. "Effect of ac Impedance on dc Voltage-Current Characteristics of Superconductor Weak-Link Junctions". In: *J. Appl. Phys.* 39.7 (1968), pp. 3113–3118.

[22] W. C. Stewart. "CURRENT-VOLTAGE CHARACTERISTICS OF JOSEPHSON JUNCTIONS". In: *Appl. Phys. Lett.* 12.8 (1968), pp. 277–280.

[23] G. Stan, S. B. Field, and J. M. Martinis. "Critical Field for Complete Vortex Expulsion from Narrow Superconducting Strips". In: *Phys. Rev. Lett.* 92.9 (2004).

[24] J. Luomahaara. *Field-tolerant SQUID sensors for a hybrid MEG-MRI system*. Master's thesis, Helsinki University of Technology, 2009.

[25] L. Grönberg et al. "Side-wall spacer passivated sub-μm Josephson junction fabrication process". In: *Supercond. Sci. Technol.* 30.6 (2017).

[26] M. Kiviranta et al. "Multilayer Fabrication Process for Josephson Junction Circuits Cross-Compatible Over Two Foundries". In: *IEEE Trans. on Appl. Supercond.* 26.6 (2016).

[27] M. Kiviranta et al. "Two-Stage SQUID Amplifier for the Frequency Multiplexed Readout of the X-IFU X-Ray Camera". In: *IEEE Trans. on Appl. Supercond.* 31.5 (2021).

[28] Bluefors. *LD Dilution Refrigerator Measurement System*. 2024. URL: https://bluefors.com/products/dilution-refrigerator-measurement-systems/ld-dilution-refrigerator-measurement-system/#technicalspecifications (visited on 05/06/2024).

[29] T. Minotani, K. Enpuku, and Y. Kuroki. "Effect of capacitive feedback on the characteristics of direct current superconducting quantum interference device coupled to a multiturn input coil". In: *J. Appl. Phys* 82.1 (1997), pp. 457–463.

[30] Wikipedia. *Barkhausen stability criterion*. 2024. URL: https://en.wikipedia.org/wiki/Barkhausen_stability_criterion#:~:text=Barkhausen%27s%20criterion%20is%20a%20necessary,but%20is%20silent%20about%20oscillation. (visited on 05/06/2024).

[31] D. Vili. “presentation 3EPo1C-06 accepted, Applied Superconductivity Conference”. In: Salt Lake City, Utah, USA (1 – 6 September 2024).

[32] M. A. Galí Labarias and E. E. Mitchell. “Numerical Study of SQUID Array Responses Due to Asymmetric Junction Parameters”. In: *IEEE Trans. on Appl. Supercond.* 33.5 (2023).

[33] R. P. Welty and J. M. Martinis. “A series array of DC SQUIDs”. In: *IEEE Trans. on Mag. Supercond.* 27.2 (1991), pp. 2924–2926.

Summary

In this Master's Thesis VTT DC SQUID arrays were measured and their IV- and ΦV- characteristics were studied and analysed. Key findings of this thesis show that the correlation between the theoretical and experimental data exists for all the irregularities analysed. In addition, the simulations of the critical current distribution show a similar rounding effect of the IV characteristics, when compared to the irregularity observed for the actual SQUID array device.

The data and results acquired by this thesis gives enough understanding of what the potential causes of the seen irregularities are and lay a good base for the further research in this field. For studying the effect of the changes in the shunt resistance, both single cell and array of SQUIDs, with intentional errors could be fabricated and measured in the future. For the more complex analysis of the critical current distribution and affect to the general coherence in the operation of the DC SQUID arrays, more complex resistively-capacitively-shunted-junction (RCSJ) or any other type of model could be used. That a model should consider the effect of changes in *Stewart-McCumber* parameter β_c and modulation parameter β_L. In conclusion, for the further development of the study of the irregularities seen in the IV- and ΦV- characteristics of DC SQUID arrays, more work should be done and will be a part of further studies.

Abstract

The basic performance of the direct current (DC) Superconducting QUantum Interference Devices (SQUIDs) array can be determined by the analysis of the current-voltage (IV) and flux-voltage (ΦV) characteristics. Main objectives of this thesis are to analyse and simulate few of the irregularities observed among the IV- and ΦV- characteristics of the DC SQUID arrays. Irregularities induced by changes in shunt resistances and critical currents of Josephson Junctions (JJs), as well as by parasitic capacitive feedback, are analysed and explained using the literature and experimental data. Separately, simplified resistively-capacitively-shunted-junction (RCSJ) model is used to analyse, simulate and compare the phenomena of the critical current distribution amongst the single cells in the DC SQUID array. Experimental data presented and analyzed in this thesis is acquired from the thin film, niobium based, DC SQUIDs, which are designed, fabricated and measured (4.2K) at VTT Technical Research Centre of Finland.

Key findings of the thesis and the experimental work show the correlation between the theoretical and the experimental data for all the irregularities analysed. Especially, the simulations of the critical current distribution show a similar rounding effect of the IV characteristics, when compared to the irregularities observed for the real devices. In conclusion, the data and the results acquired, give enough understanding on what are the potential causes of the observed irregularities. However, for a more accurate and complete understanding, more experimental work should be done and a more comprehensive simulation model(s) should be used.

Annotatsioon

Mitmelülilise alalisvoolu ülijuhist kvantinterferomeeteri töövõimet on võimalik määrata volt-amper (IV) ja magnetvoo-volt (ΦV) karakteristikute põhjal. Peaeesmärkideks antud lõputöös on analüüsida ja simuleerida mõningaid anomaaliad, mis on esinenud mitmelülilise alalisvoolu ülijuhist kvantinterferomeetrite IV- ja ΦV- karakteristikutes. Anomaaliad on tingitud takistuse ja kriitilise voolutugevuse muutumisest *Josephsoni* siirdes (inglise keeles *Josephson Junction*), kui ka parasiitmahtuvusele põhineval, positiivsele tagasisidemele. Anomaaliate analüüsiks ja seletamiseks on kasutatud kirjandust ja mõõtmistulemusi. Eraldi on kasutatud lihtsustatud *resistively-capacitively-shunted-junction* (RCSJ) mudelit, et kirjeldada, simuleerida ja võrrelda kriitilise voolu jaotumist mitmelülilise ülijuhist kvantinterferomeetri üksikutes rakkudes. Mõõtmistulemused antud töös põhinevad alalisvoolu ülijuhist kvantinterferomeetritele, mis on töödeldud välja, mõõdetud ($4.2K$) ja toodetud Soome tehniliste uuringute keskuses (VTT Technical Research Centre of Finland) põhinedes õhukese tahkiskile tehnoloogiale, kus peamine ülijuhist metall on nioobium.

Lõputöö tulemused näitavad korrelatsiooni mõõtmistulemuste ja teoreetiliste andmete vahel, kõikide anomaaliate korral, mis on selles töös uuritud. Eriti on täheldatud, et simulatsioonid kriitilise voolu jaotumisest näitavad IV karakteristiku ümardumist, mis on väga sarnane mõõtmistulemustele. Kokkuvõtteks võib öelda, et saavutatud tulemused ja mõõtmistulemuste andmed, annavad piisava arusaama, mis põhjustab anomaaliate tekke. Teisalt selleks, et omada veelgi paremat ja kompleksemat arusaama anomaaliate tekke põhjustest, tuleks läbi viia rohkem mõõtmisi ja kasutada keerulisemat simulatsiooni mudelit.

Appendices

Appendix 1

Figure 7.1: VTTs setup used for $4.2K$ measurements, where dipstick is inserted into the *Dewar* filled with liquid helium. The top part of the dipstick is a cage where room temperature electronics are situated. Signal lines are fed from the bottom of the dipstick all the way to the room temperature electronics, inside the fiberglass tube.

Appendix 2

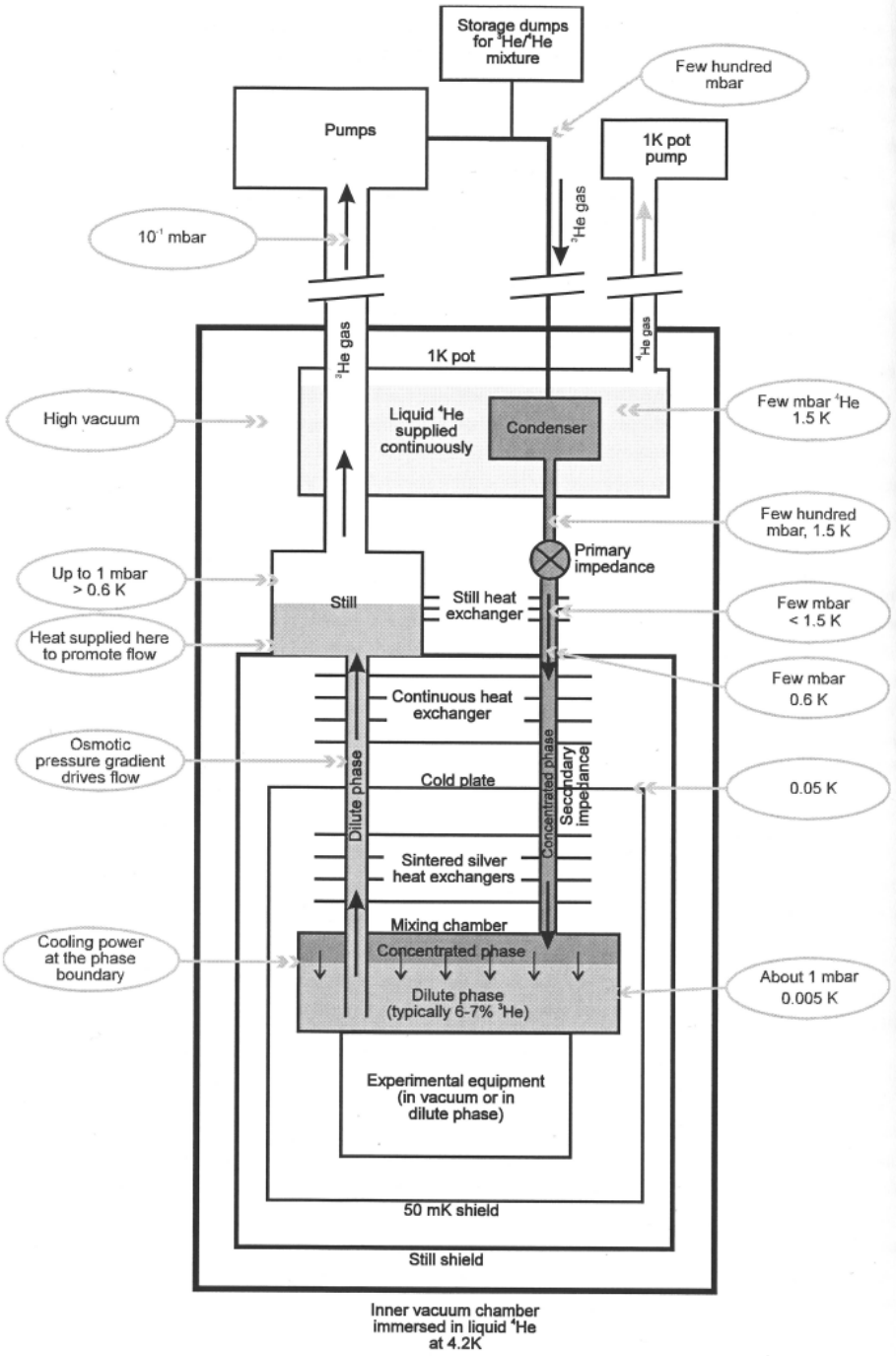

Figure 7.2: He^4/He^3 wet type dilution refrigerator [17].

Appendix 3

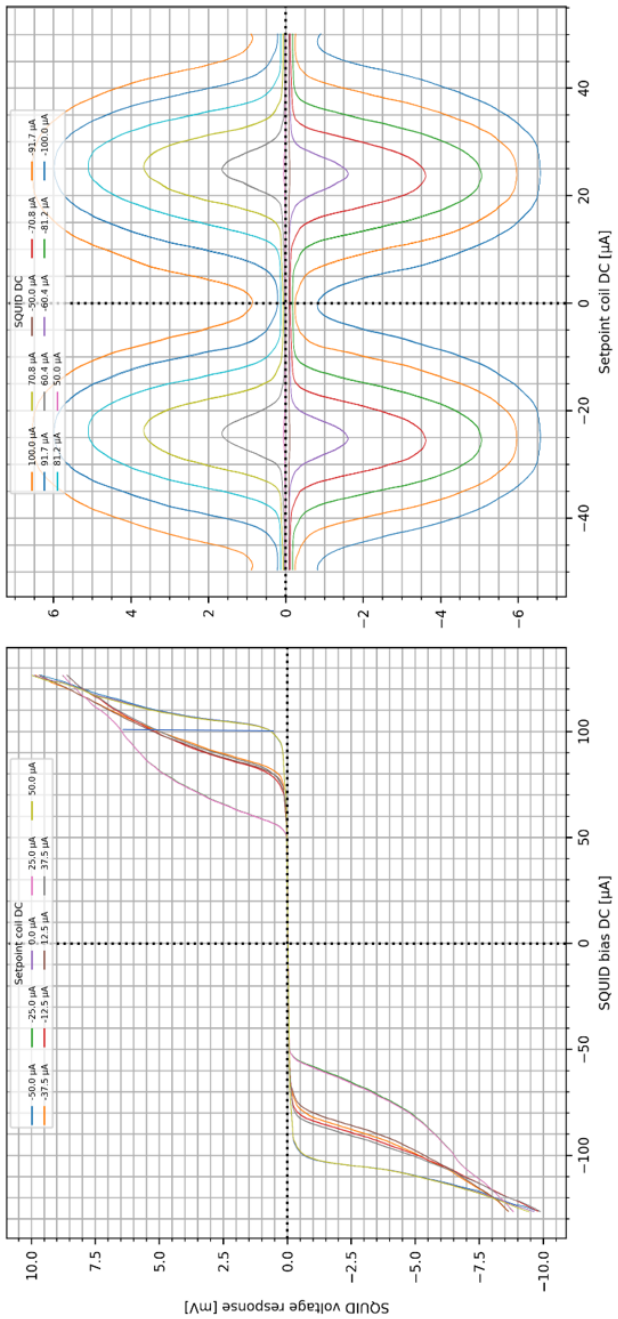

Figure 7.3: IV- (lowest plot) and ΦV- (highest plot) characteristics of 4x40 array VTT SQUID.

Appendix 4

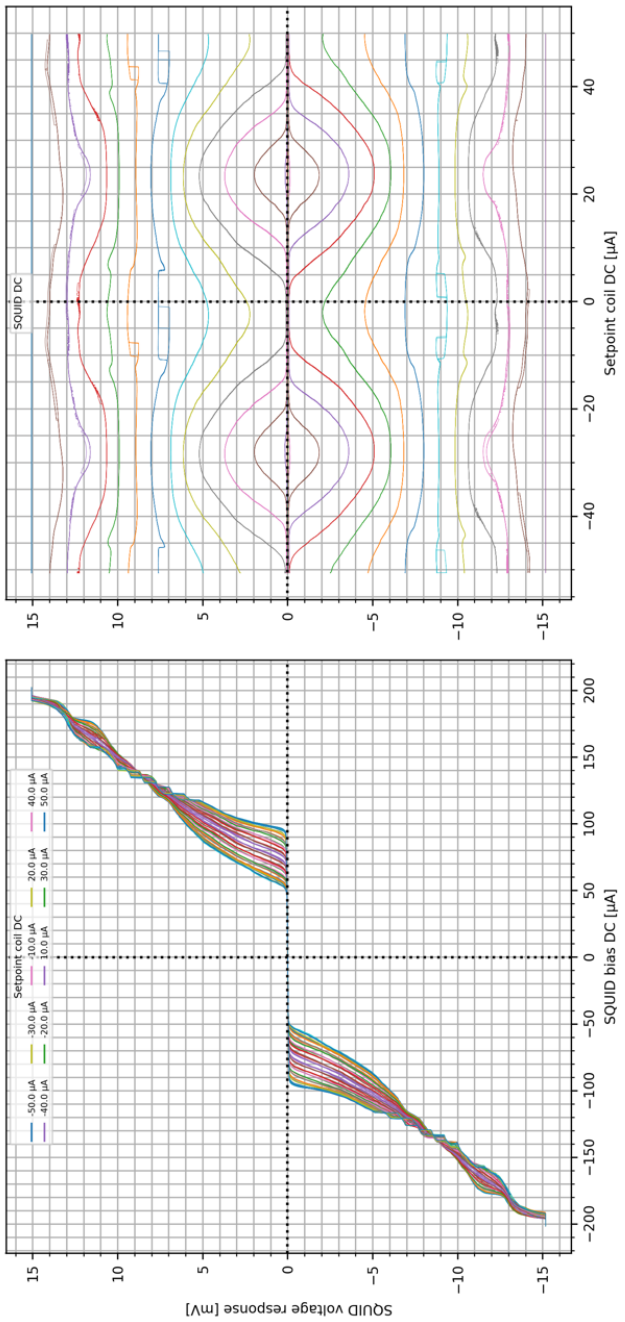

Figure 7.4: IV- (lowest plot) and ΦV- (highest plot) characteristics of 4x40 array VTT SQUID.

Appendix 5

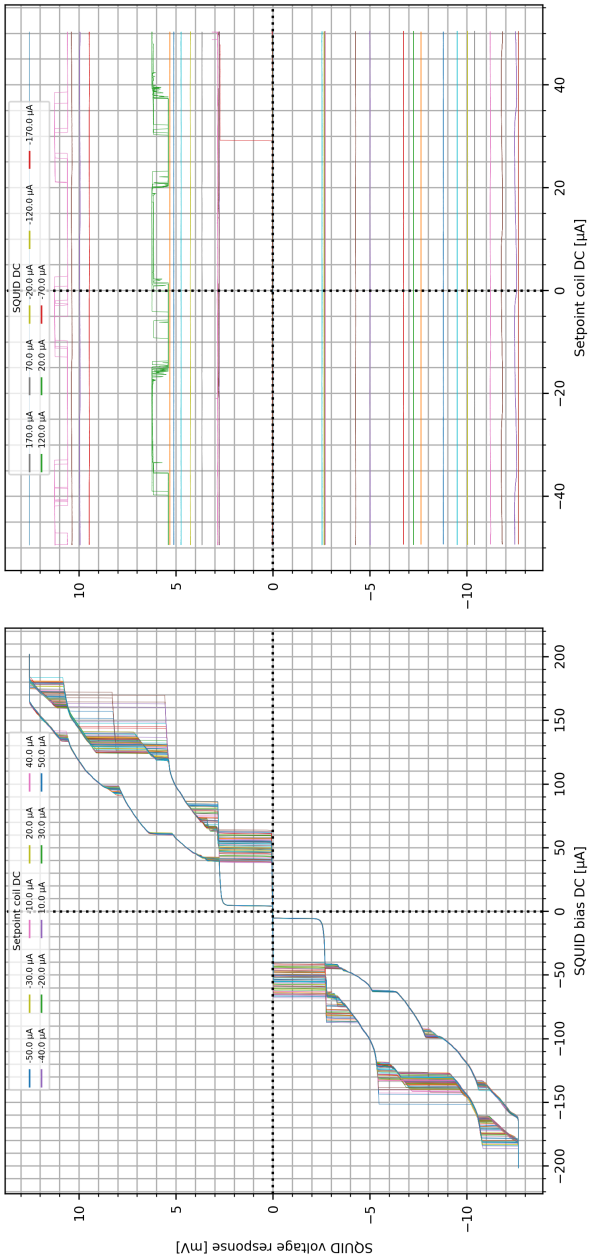

Figure 7.5: Hysteresis seen in the IV- (lowest plot) and ΦV- (highest plot) characteristics of 4x40 array VTT SQUID.

Appendix 6

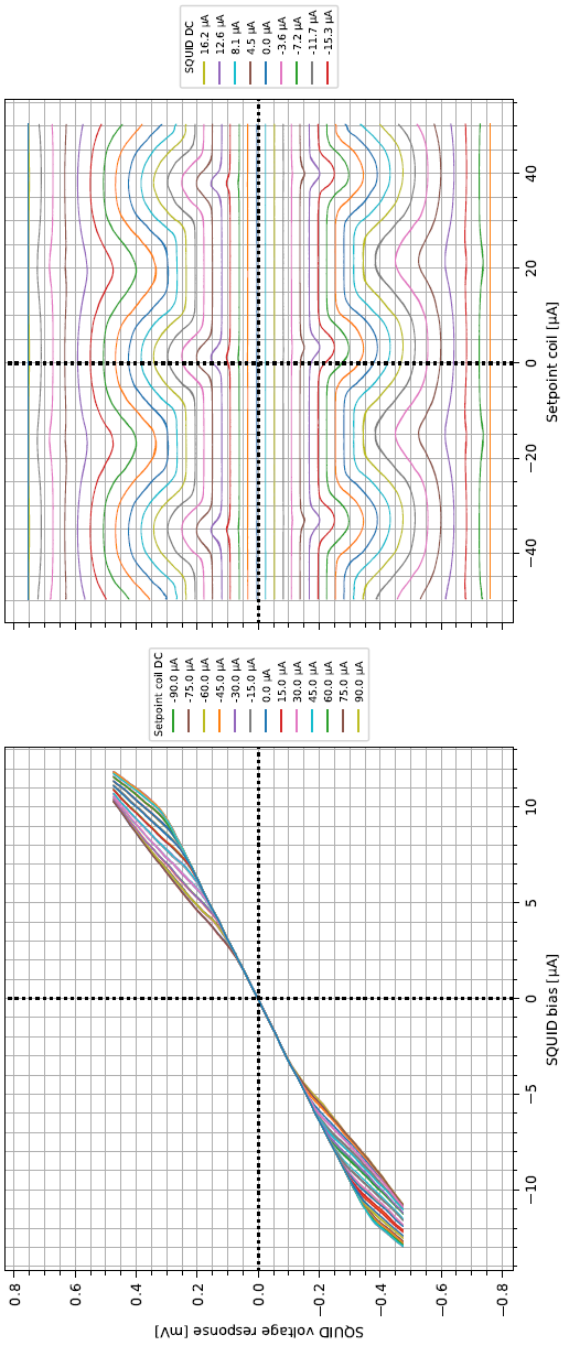

Figure 7.6: IV- (lowest plot) and ΦV- (highest plot) characteristics of 1x2 array VTT SQUID. Indicating at least one of the SQUID cells with damaged JJ structures.

Appendix 7

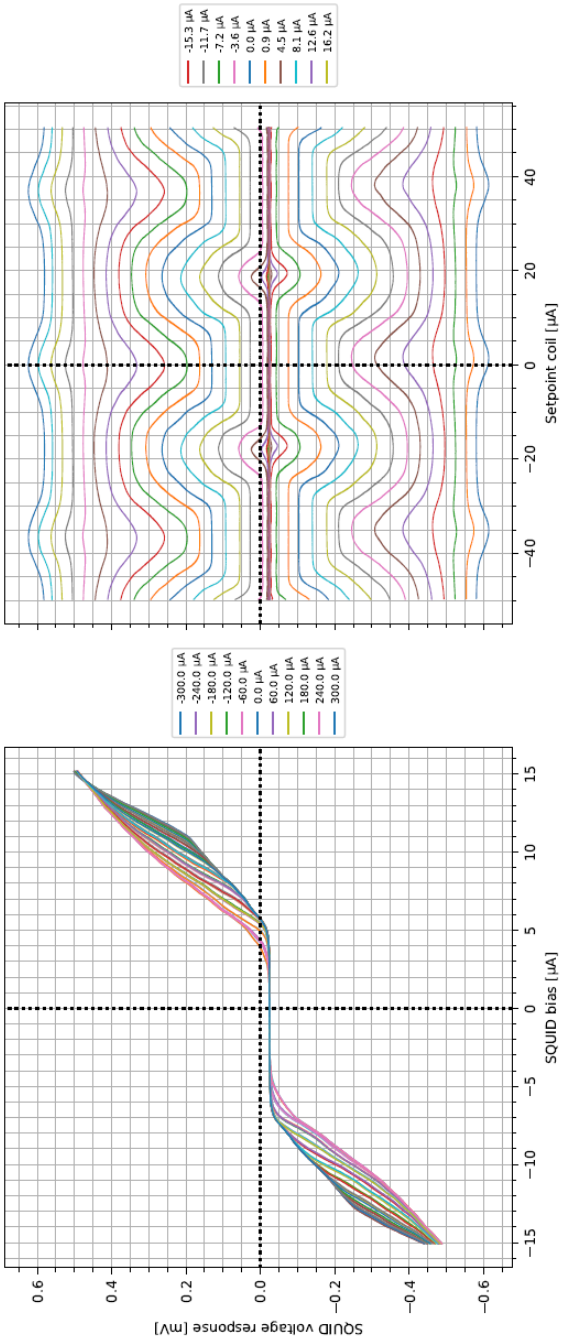

Figure 7.7: IV- (lowest plot) and ΦV- (highest plot) characteristics of 1x2 array VTT SQUID. Different critical currents among individual SQUID cells.

Appendix 8

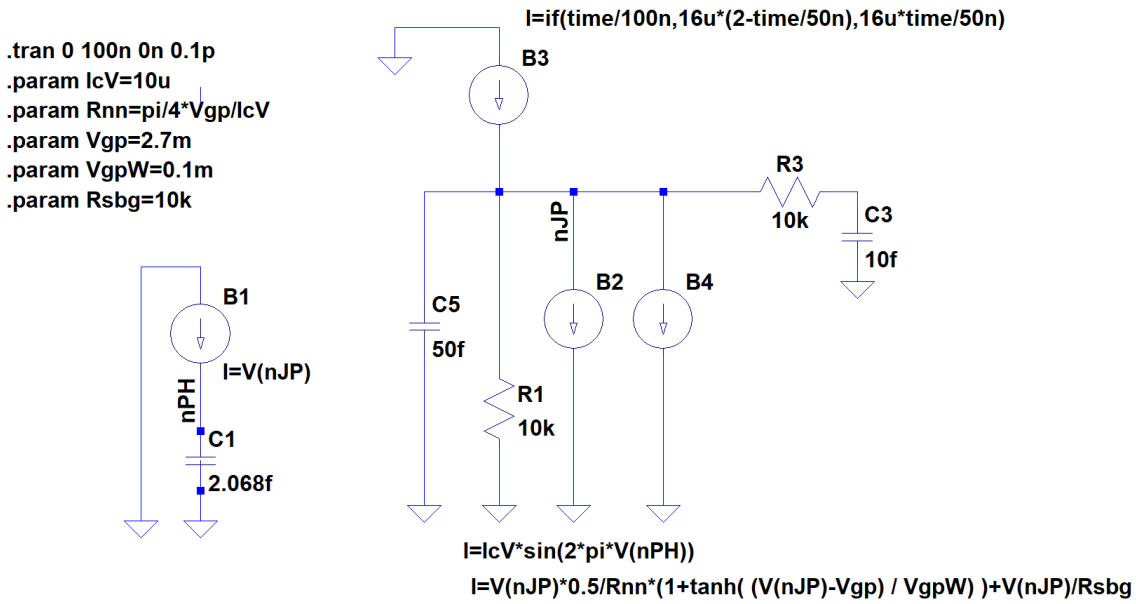

Figure 7.8: *LTspice* model used to simulate β_c changes induced by resistance change.

Appendix 9

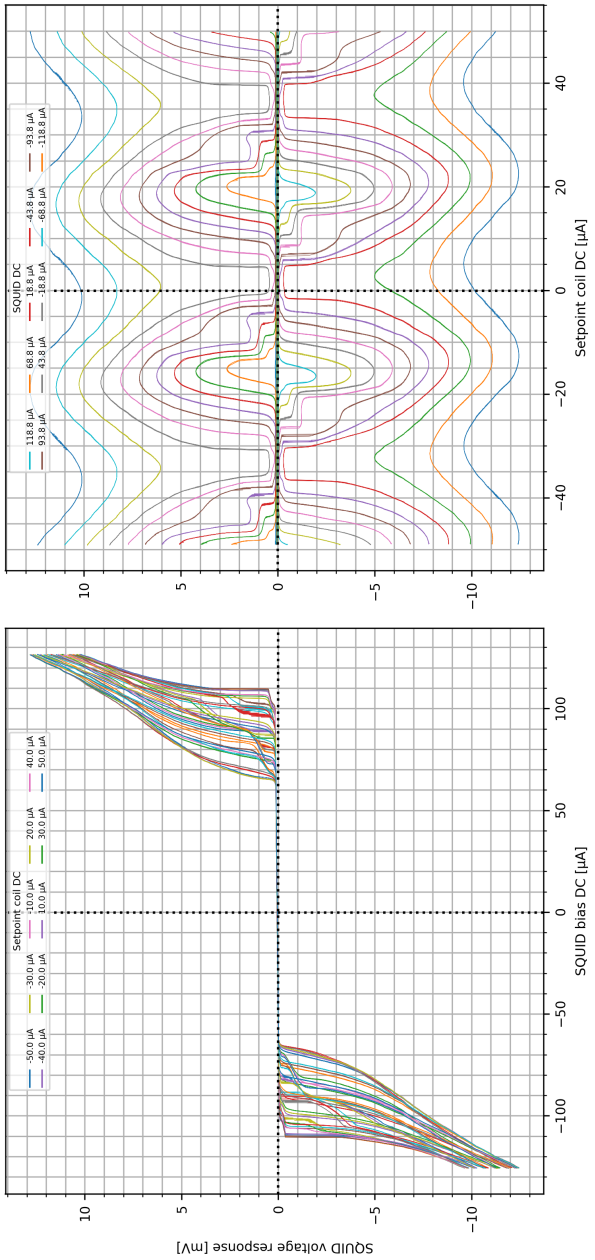

Figure 7.9: IV- (lowest plot) and ΦV- (highest plot) characteristics of 4x40 VTT SQUID measured with the setup suspected to have parasitic capacitance.

Appendix 10

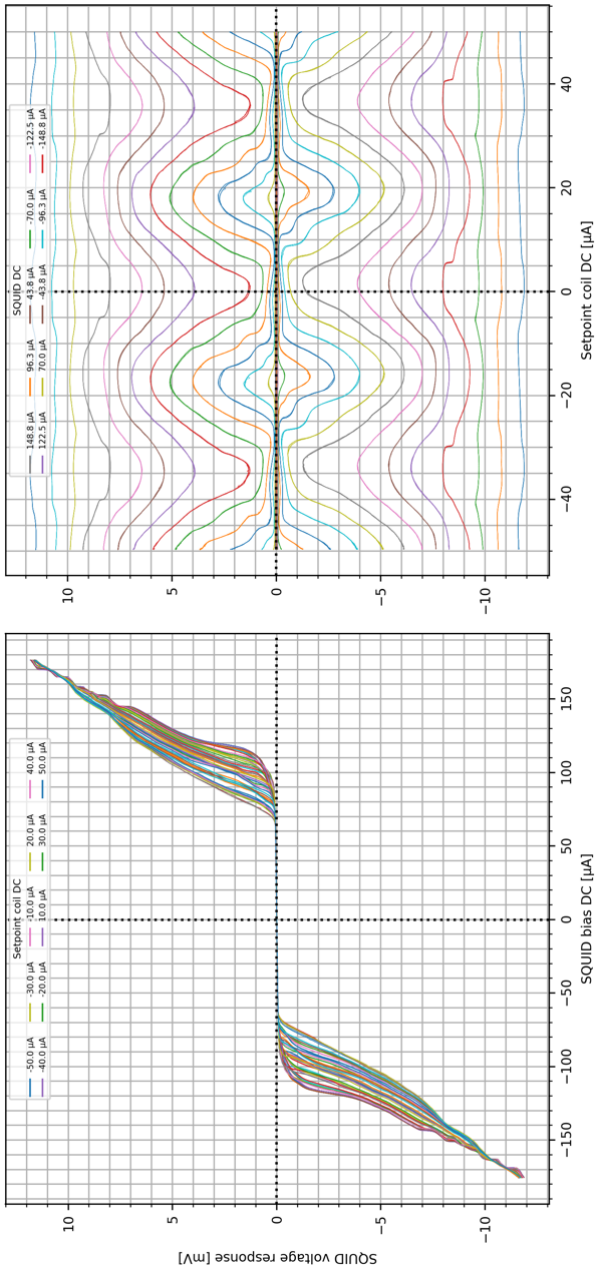

Figure 7.10: IV- (lowest plot) and ΦV- (highest plot) characteristics of 4x40 VTT SQUID with the rounded transition from the superconducting to finite-voltage state.

Appendix 11

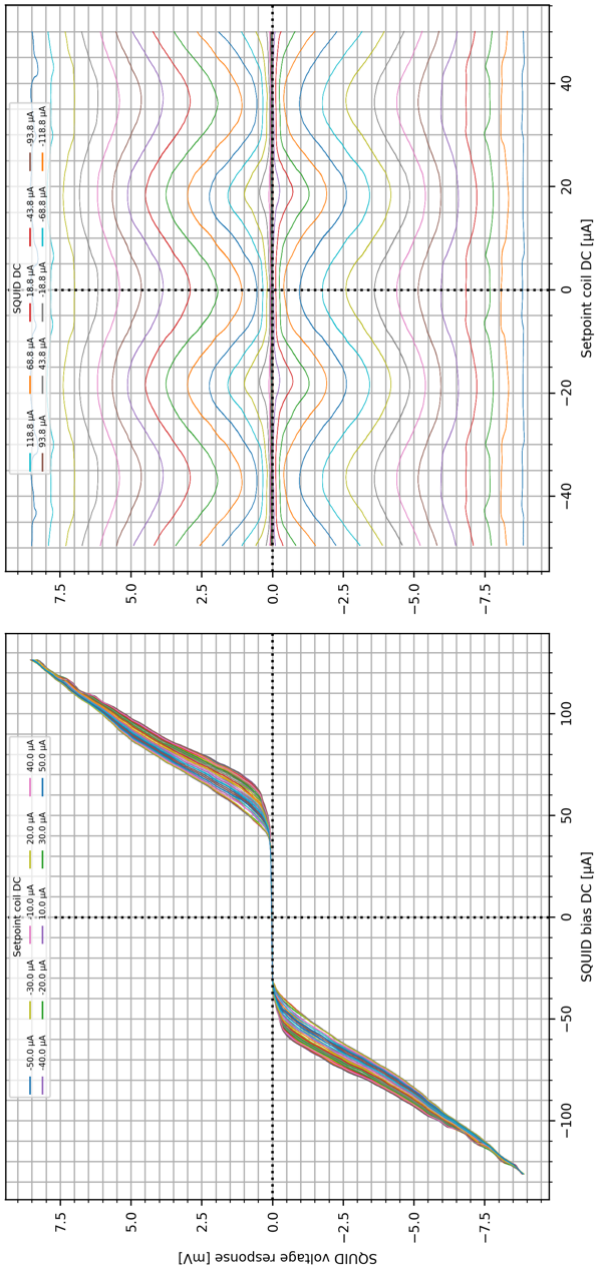

Figure 7.11: IV- (lowest plot) and ΦV- (highest plot) characteristics of 4x40 VTT SQUID with the suspected trapped flux.

Appendix 12

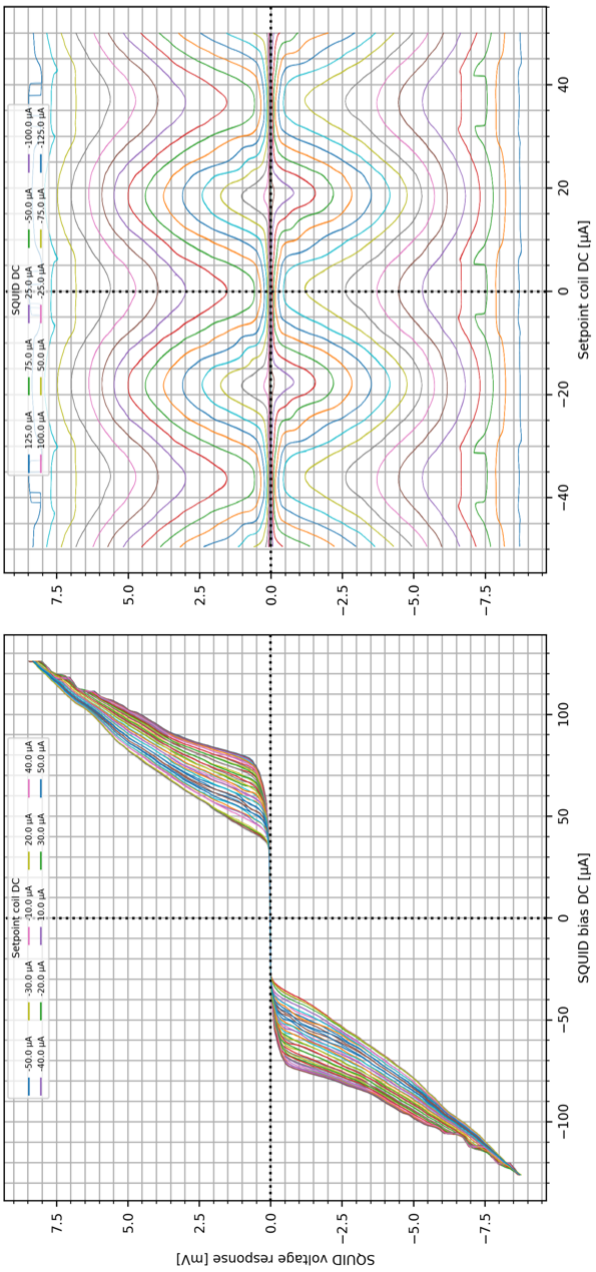

Figure 7.12: IV- (lowest plot) and ΦV- (highest plot) characteristics of 4x40 VTT SQUID after the heat pulsing to get rid of the trapped flux, as seen in the Appendix [9].

Appendix 13

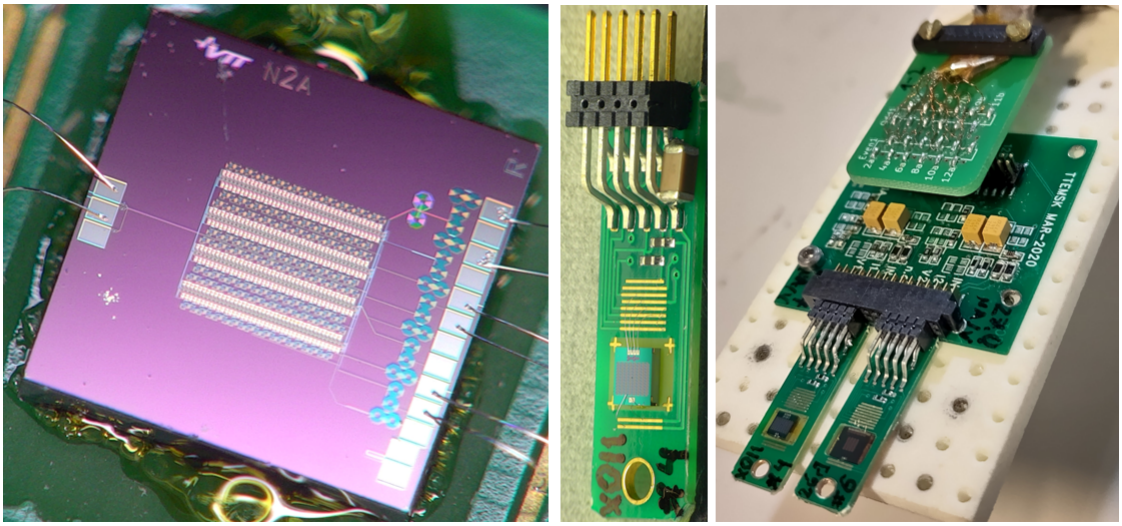

Figure 7.13: (Left) A 4 x 40 SQUID array, fabricated with thin film technologies on a 4 x 4 mm chip in the VTT/Micronova clean room, of the type used in experiments in this thesis. (Middle) A SQUID carrier board, with a SQUID array chip attached and wire bonded. The attached chip is different construction from the 4 x 40 SQUID array. Also visible is an external SMD capacitor, of a type tolerating T = 4.2 K temperature, soldered to connector pins. A similar capacitor, soldered on different pins have been used as the feedback element in the tests of the section 6.2 . (Right) The cold adapter board, with two SQUID carriers plugged in. The board will be immersed in liquid helium by using a dipstick.

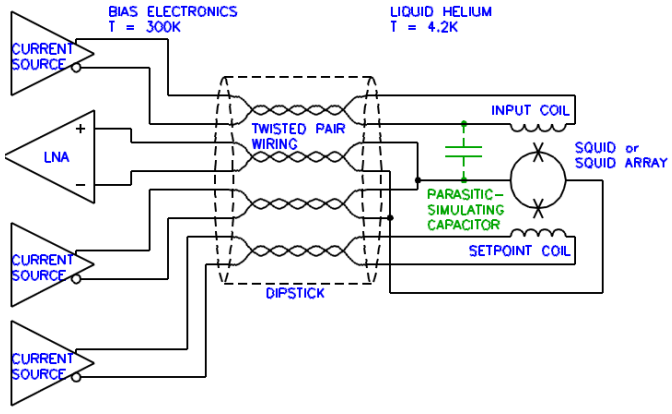

Figure 7.14: Schematic diagram of the experiment described in section 6.2.

Annex
to Rector's directive No 1-8/17 of 7 April 2020

Non-exclusive licence for reproduction and publication of a graduation thesis[1]

I Daniil Vili

1. grant Tallinn University of Technology free licence (non-exclusive licence) for my thesis *Irregularities seen in the electrical characteristics of a large array direct current Superconducting Quantum Interference Devices due to the deviations in the single cell parameters*

supervised by Mikko Kiviranta and Mihhail Klopov

1.1 to be reproduced for the purposes of preservation and electronic publication of the graduation thesis, incl. to be entered in the digital collection of the library of Tallinn University of Technology until expiry of the term of copyright;

1.2 to be published via the web of Tallinn University of Technology, incl. to be entered in the digital collection of the library of Tallinn University of Technology until expiry of the term of copyright.

2. I am aware that the author also retains the rights specified in clause 1 of the non-exclusive licence.

3. I confirm that granting the non-exclusive licence does not infringe other persons' intellectual property rights, the rights arising from the Personal Data Protection Act or rights arising from other legislation.

14/05/2024

[1] The non-exclusive licence is not valid during the validity of access restriction indicated in the student's application for restriction on access to the graduation thesis that has been signed by the school's dean, except in case of the university's right to reproduce the thesis for preservation purposes only. If a graduation thesis is based on the joint creative activity of two or more persons and the co-author(s) has/have not granted, by the set deadline, the student defending his/her graduation thesis consent to reproduce and publish the graduation thesis in compliance with clauses 1.1 and 1.2 of the non-exclusive licence, the non-exclusive license shall not be valid for the period.